

Research Attachment
Institute of High Performance Computing, A*STAR, Singapore

Summary Report

Atomistic Simulation of Inhibition of Paraffin Crystal Growth



Institute of
High Performance
Computing

Shi-Lin WANG

Master Student, Ecole Polytechnique Federale de Lausanne, Lausanne, Switzerland

Supervisors: Dr. David WU

August 2019 - January 2020

Contents

Contents	1
List of Figures	2
List of Tables	2
1 Overview	3
2 N-alkane	4
2.1 Crystal Structure of N-alkane	4
2.2 Solid-State Mesophase	4
2.3 Mechanism of N-alkane Crystallization	4
3 Coarse-Grain Model	8
3.1 Introduction	8
3.2 Design Force-Field for Coarse-Grain Model	8
3.3 Different Coarse-Grain Model	9
3.4 Preliminary Screening of Coarse-Grain Models	10
4 Details of Selected Coarse-Grain Models	11
4.1 Coarse-Grain Model Parameters	11
4.2 Liquid Density Simulation	14
4.3 Melting Point Simulation	15
4.3.1 Direct Heating/ Cooling Method	15
4.3.2 NPH Simulation	16
4.4 CG models' Performance	18
4.5 Selection of CG models	20
5 Study of Crystal Growth	21
5.1 Averaged Local Bond Order Parameter (\overline{Q}_l)	21
5.2 Rate of Crystal Growth	21
5.3 Crystal Growth Mechanism	25
5.4 Introducing Inhibitors into the System	27
5.4.1 Inhibitor Density Simulation	27
5.4.2 Effect of Inhibitor on the Octacosane System	29
6 Conclusion	31
References	33

List of Figures

1	HTGC analysis of crude oil	3
2	Pipeline segments with solid deposits	3
3	Example of rotator phase.	6
4	Free energies as a function of the length of n-alkane	7
5	Snapshots of the time evolution of a n-alkane chain.	7
6	Snapshots of single row of molecules	8
7	Schematic figure of different CG resolution	10
8	Plot of CG potential	12
9	LAMMPS defintion of dihedral angle Φ	12
10	Lennard-Jones potential	14
11	Input structure for the liquid density simulation	14
12	Liquid density simulation result for slected CG models	15
13	Final crystal structure from cooling process	16
14	Simulation result of direct (a)heating / (b)colling method for RR	17
15	Typical P-H diagram of water	17
16	Input structure for the NPH simulation	18
17	NPH simulation result for RR	19
18	NPH simulation result for TraPPE-UA	19
19	Performance (P) vs Number of molecule (N) for RR and TraPPE-UA	20
20	Initial structure for the crystal growth simulation at 0ns	22
21	Time evolution of crystal growth	23
22	Crystallinity distribution along x-direction for different time	24
23	Crystal length evolution vs. time for TraPPE	24
24	Crystal length evolution vs. time for RR	25
25	Bead-wise Q_6 evolution for example, molecule no. 139	26
26	Bead-wise \overline{Q}_6 evolution for example, 20 different molecules	26
27	Histogram of preferred attaching bead site for RR and TraPPE; Error-bar represents the standard errors for each corresponding beads	27
28	Example inhibitors for (a)linear- / (b)comb- shaped molecule	28
29	EVA molecule (31.5% vinyl acetate) for the inhibitor simulation	28
30	Inhibitor density simulation of EVA (31.5% vinyl acetate) for different CG-models	29
31	EVA molecule (29.3% vinyl acetate) for the inhibitor simulation	31
32	Snapshot of EVA molecule (31.5% vinyl acetate) at 30 ns	32
33	Snapshot of EVA molecule (29.3% vinyl acetate) at 30 ns	32
34	Q_6 colored snapshot of EVA molecule (29.3% vinyl acetate) at 30 ns	33

List of Tables

1	Crystal structure of n-alkanes	5
2	List of three categories of CG model resolution and their corresponding force-field	9
3	Direct cooling/ heating simulation result	10
4	Details of potential RR, DR & TraPPE	13
5	Table of comparison between RR and TraPPE-UA	20
6	Rate of crystal growth for TraPPE and RR	25
7	Definition for the start/ end of crystallization	27
8	Details of TrapPE abbreviation for EVA bead type	29
9	Details of TrapPE pair potentials (12-6 LJ potential) for EVA	30
10	Details of TrapPE bond potentials $k_b(b - b_0)$ for EVA	30
11	Details of TrapPE angle potentials $k_\theta(\theta - \theta_0)$ for EVA	30
12	Details of TrapPE dihedral potentials (LAMMPS-opls type potential) for EVA	30
13	Details of TrapPE dihedral potentials (LAMMPS-fourier type potential) for EVA	30
14	Comparison between two EVA inhibitor molecules	31

1 Overview

Crude oil is the necessity in our current generation. It consists of various components, such as paraffin, resins, bitumens, aromatics, naphthenes and etc. Figure-1 shows one high-temperature-gas-chromatogram analysis (HTGC) result of crude oil by N. X. Thanh et al [1]. As the progress of technology, it becomes feasible now for the crude oil exploration and production in locations that were not considered economically viable in the past. For example, the use of sub-sea transportation has already been deployed for the offshore oil production. However, because of the cold environments and the long transportation distances, crude oil precipitation and deposition has become an inevitable issue.

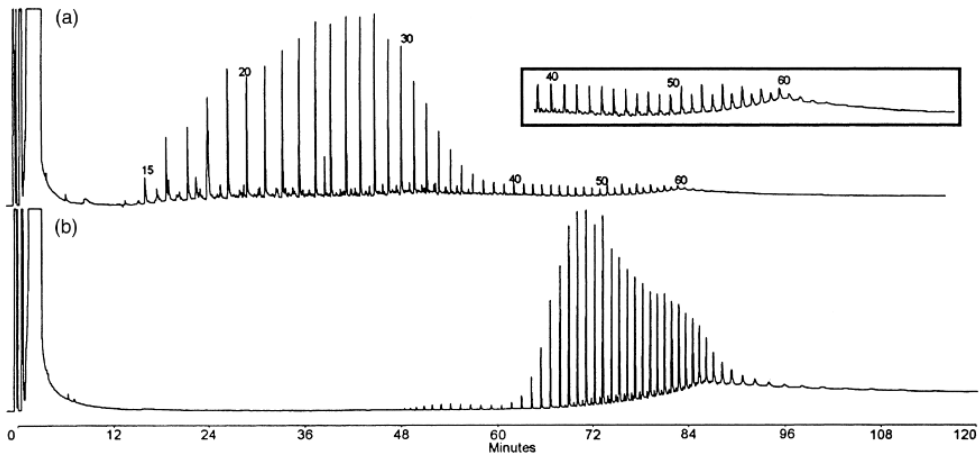


Figure 1: HTGC analysis of crude oil

(a) Crude oil from Uinta Basin (b) Asphaltene isolated from the crude oil used for (a) and isolated by the classical pentane precipitation method

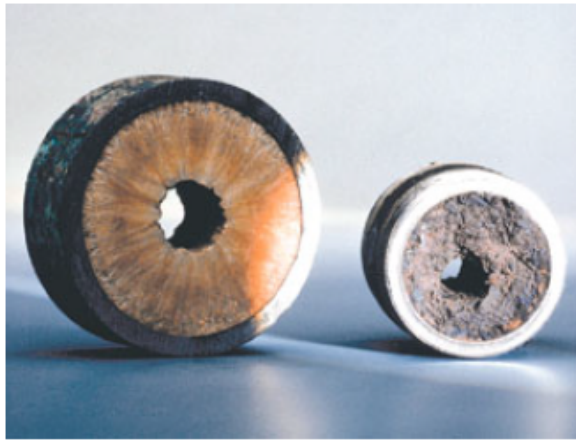


Figure 2: Pipeline segments with solid deposits

Among the components of crude oil, high molecular weight n-paraffins or asphaltenes are notorious pipe-cloggers. They are normally less profitable due to their lower energy accessibility and often condense on production equipment wall when temperature is lower or close to ambient. Such precipitation and deposition will reduce the pipeline diameter or even eventually plug it completely as shown by Figure-2. Researchers have investigated different methods to inhibit the deposition process. They are divided into physical and chemical methods. For physical methods, they include heat insulation, frequent heating, mechanical remediation techniques, internal pipeline coating and etc. On the other hand, chemical methods include different kinds of inhibitor such as ethylene copolymers, comb polymers, dispersants. Normally, designing an efficient chemical inhibitor requires either some insights or extensive try-and-errors. Therefore, to speed up the exploration or simply to screen out the not-worth-trying chemicals, the goal is to examine and understand the whole details of such process.

Besides doing experiments, the computer simulation provides a powerful tool to analyse the crystallization process even to the level of electronic or atomic scale. Nonetheless, it takes a great amount of calculation time which makes it impossible for such complicated system. Therefore, in this project, we conduct Coarse-Graining Molecular-Dynamics simulation with open-source software "LAMMPS" [2] aiming to increase the efficiency while maintaining the fidelity. From Figure-1 (a), it can be observed that most of the molecules in crude-oil roughly ranges from $C_{15}H_{32}$ to $C_{40}H_{82}$. Therefore, starting from basic, we choose the homogeneous normal alkane "Octacosaneas $C_{28}H_{58}$ " as the ensemble constituent because it is representative enough which peaks in the Figure-1 (a). In this report, normal alkane and Coarse-Graining model are first introduced (section-2 and 3). Best-suited Coarse-Graining force-field and the nucleation process for octacosaneas are covered afterward (section-4). Finally, the effect of chemical inhibition will be investigated (section-5).

2 N-alkane

2.1 Crystal Structure of N-alkane

Normal alkanes (N-alkanes) crystallize to form thin plates with regular faces in which the chain is more or less perpendicular to the lamella surface. Previously the basic crystallography information is only limited to a number of pure n-alkanes. New study by S. R. Craig et al[3] has determined the unit-cell parameters of n-alkanes within the range $C_{13}H_{28} - C_{60}H_{122}$ by high-resolution X-ray powder diffraction using synchrotron radiation. All the measurements were carried under ambient condition (except for n-alkane with $n < 18$, which melt readily).

They found the difference in the structure between the odd- and even- length n-alkanes arises due to the packing of the terminal methyl groups. For the odd-length n-alkanes the terminal methyl groups pack in the same direction (the two terminal methyl groups are on the same side with respect to the main carbon chain), whereas for the even-length n-alkanes they produce in opposite directions. The overall results are listed in Table 1. For the shorter even n-alkanes, terminal methyl-methyl interaction dominates the packing and makes the formation of a unimolecular triclinic lattice. As the even chain length increases, the interactions between chains begin to overtake the effect from the terminal forces. Thus at $C_{28}H_{58}$ and at $C_{36}H_{74}$, the unit-cell incrementally adopting a more orthogonal lattice by transforming to bi-molecular monoclinic and tetra-molecular orthorhombic unit-cell. On the other had, for the odd-length alkanes, the mirror symmetry of the molecule tends to preclude optimal close packing and the unit-cell is tetra-molecular orthorhombic.

From Table-1, there are two phases all corresponding to C_{36} . It reveals the polymorphic behavior of $C_{36}H_{74}$. These structures exhibit the same herringbone-type packing motif. The only difference is that there is a single alkane chain aligning along c-axis for the Monoclinic phase unit-cell.

2.2 Solid-State Mesophase

During the crystallization of n-alkanes, one distinct type of phase called 'rotator phase' will occur depending on the cooling rate and the length of n-alkane. For example, different rotator phases into which crystallization actually occurs are R_I (distorted hexagonal) for $n \leq 21$, R_{II} (hexagonal) for $21 \leq n \leq 26$, and R_{IV} (tilted) for $n \geq 26$. Rotator phases are weakly ordered crystallized phases occurring (in equilibrium) at temperature between the liquid phase and the melt. They are crystals which lack long-range order with respect to rotation about the long axis of the molecule, shown as Figure-3, and they play a role in the nucleation of the n-alkane. Experiment suggested that n-alkanes crystallize from the melt via the nucleation of a rotator phase [4]. Detailed atomistic simulation has also been carried [5].

2.3 Mechanism of N-alkane Crystallization

Similar to most crystallization process, n-alkane experiences nucleation and growth. Supersaturation causes the nucleation, which are formation and agglomeration of molecular solute clusters. These clusters are maintained in a dynamic equilibrium which is dictated by the balance between the volume and surface contribution to their excess free energy. Besides crystallization direct into stable solid phase such as short length n-alkane, the nucleation of n-alkane from the melt could occur into a rotator transient phase that converts to the stable form during some stage of growth. E. B. Sirota et al. [6] has used time

C_nH_{2n+2}	lattice system	space group
13	Orthorhombic	$Pbcm$
14	Triclinic	$P\bar{1}$
15	Orthorhombic	$Pbcm$
16	Triclinic	$P\bar{1}$
17	Orthorhombic	$Pbcm$
18	Triclinic	$P\bar{1}$
19	Orthorhombic	$Pbcm$
20	Triclinic	$P\bar{1}$
21	Orthorhombic	$Pbcm$
22	Triclinic	$P\bar{1}$
23	Orthorhombic	$Pbcm$
24	Triclinic	$P\bar{1}$
25	Orthorhombic	$Pbcm$
26	Triclinic	$P\bar{1}$
27	Orthorhombic	$Pbcm$
28	Monoclinic	$P2_1/a$
29	Orthorhombic	$Pbcm$
30	Monoclinic	$P2_1/a$
31	Orthorhombic	$Pbcm$
32	Monoclinic	$P2_1/a$
33	Orthorhombic	$Pbcm$
34	Monoclinic	$P2_1/a$
35	Orthorhombic	$Pbcm$
36	Monoclinic	$P2_1/a$
36	Orthorhombic	$Pca2_1$
37	Orthorhombic	$Pbcm$
38	Orthorhombic	$Pbca$
40	Orthorhombic	$Pbca$
41	Orthorhombic	$Pbcm$
44	Orthorhombic	$Pbca$
46	Orthorhombic	$Pca2_1$
50	Orthorhombic	$Pca2_1$
60	Orthorhombic	$Pca2_1$

Table 1: Crystal structure of n-alkanes

The range between $C_{28}H_{58}$ and $C_{36}H_{74}$ is indicated by the horizontal lines. For even-length n-alkane, there is a transition from Triclinic unit-cell, Monoclinic unit-cell to Orthorhombic unit-cell.

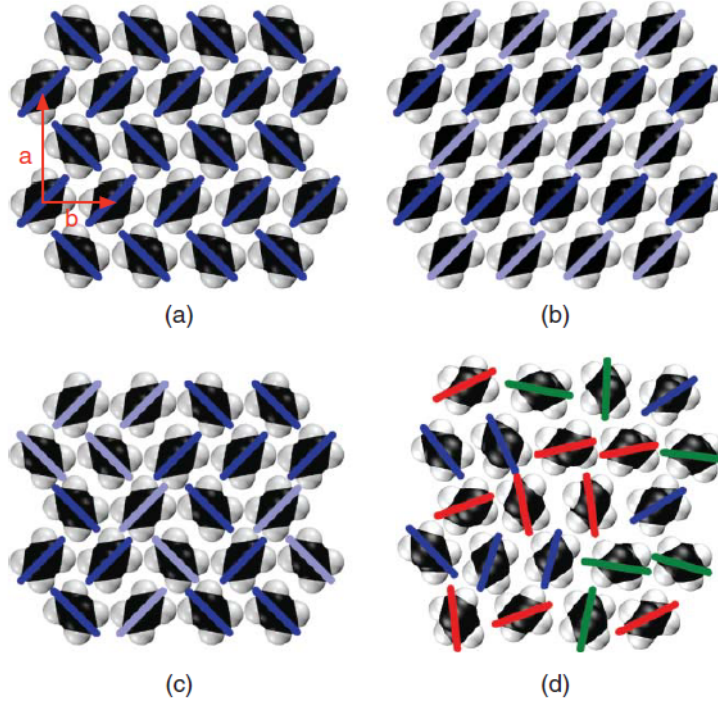


Figure 3: Example of rotator phase.

(a) Orthorhombic herringbone crystal; (b) Monoclinic crystal; (c) Orthorhombic R_I rotator phase; (d) Hexagonal R_{II} phase

resolved X-ray scattering to find a transient metastable rotator phase occurs on the crystallization of n-alkane (C_{13} to C_{25}) into their triclinic crystal structure. The nucleation kinetics and the structure-kinetic inter-relationship are also been studied by A. M. Taggart et al. [7] by differential thermal analysis.

Despite many research efforts, it still remains experimentally unknown about the actual mechanism of n-alkane crystallization at the atomic level. However, as mentioned in section-1, recent computer simulation provides an ideal instrument to complement such inability. M. Anwar et al. [8] studied the homogeneous crystal nucleation and growth of crystallization in a model system for eicosane (C_{20}) by means of molecular dynamics simulation. Although it cannot provide a mechanism which suits for all n-alkanes, this offers an insight for us into the crystallization of n-alkane. They use standard united-atom model for polyethylene in which $-CH_2-$ and $-CH_3$ are represented as different groups. 500 chains of $C_{20}H_{22}$ are equilibrated at temperature $T = 400K$ isobarically $P = 1$ atm and then are quenched to $T = 250K$, where the homogeneous crystal nucleation and growth are observed.

- During the nucleation process, they found the critical nucleus size is of $80 \pm 20 -CH_2-$ beads and the nucleation process is completed by straightening of the chains in cluster. As shown by Figure-4, reflected by the associated free energy, aligned clusters segments of more than 9 chains are unlikely to appear by spontaneous fluctuation. In contrast, straightened chains have relatively low energy and thus have higher probabilities to be found in the melt, where up to 14-15 out of 20 segments can point in the same direction. However, in the melt the chains are sufficiently prolate to undergo an ordering transition. They start straightening once an oriented cluster is formed. It is because the study found the averaged radius of gyration and the local density start to increase when it is approaching the formation of critical nucleus.
- Once a stable nucleus is formed, crystal growth proceeds via the successive attachment of new chains and a lamellar structure develops. The simulation result shows that the initial stages of the attachment process are driven by the motion of the most mobile chain segments and that the crystallization of new chains is initiated at the ends. However, this is only specific to short chains, and is in contrast to folded chain crystallization for longer chains. Figure-5 shows the detailed process for n-alkane cluster growth. As it shows, the end of a chain is attached on the lateral

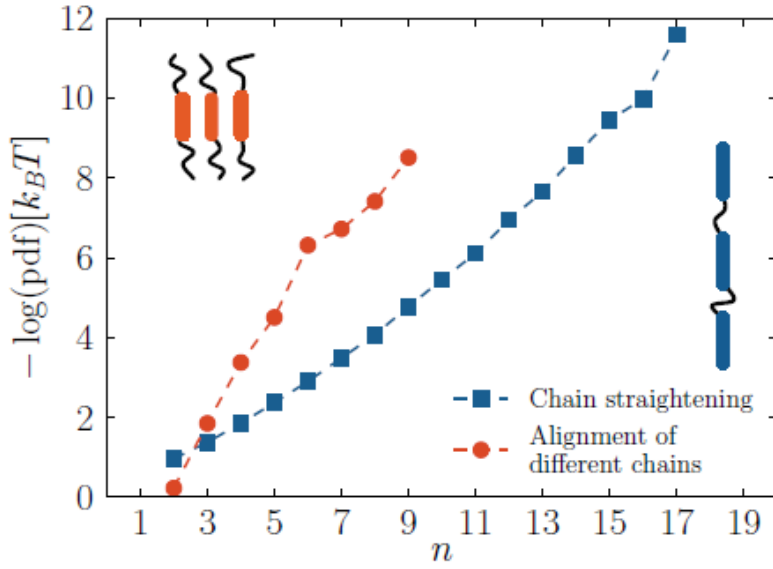


Figure 4: Free energies as a function of the length of n-alkane

The free energies for straightening of individual chains (blue) and for alignment chains (red) as a function of the length of n-alkane. The colored segments in the sketches represent the selection criteria for the computation of the corresponding probabilities.

surface of the cluster. The end particle 'slides in' lateral surface and increases the local order of neighboring particles. Then with the same manner, these particles enter the region one by one and the attached chain is in a L-shaped conformation before the chain fully crystallized.

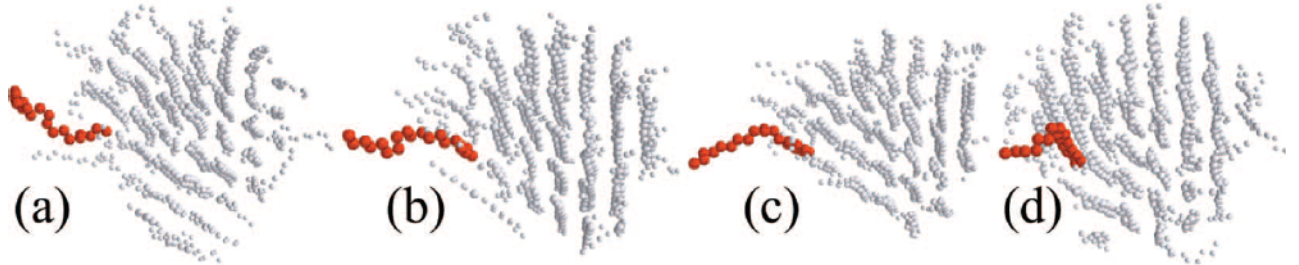


Figure 5: Snapshots of the time evolution of a n-alkane chain.

A 'slides-in' process is shown as the molecule (red colored) gradually attaches the alkane crystal. (a-d)

As mentioned previously, the nucleation of n-alkane could occur into a rotator transient phase. N. Wentzel et al. [9] used computer simulation to study the rotator phase transitions of N-alkane $C_{23}H_{48}$ from Orthorhombic- R_I to $R_I - R_{II}$. They found that the R_I phase is well described as an orthorhombic crystal disordered by random $\pm 90^\circ$ rotations of molecules about their stem axis, and the R_{II} phase can be represented as a loose hexagonal packing of parallel chain stems, which tend to orient with the in-plane projection of C – C bonds between neighbors (See Figure-3). As shown by Figure-3 and -6, the mechanism is mainly driven by thermal fluctuation and the movement of chains is mainly confined in-plane.

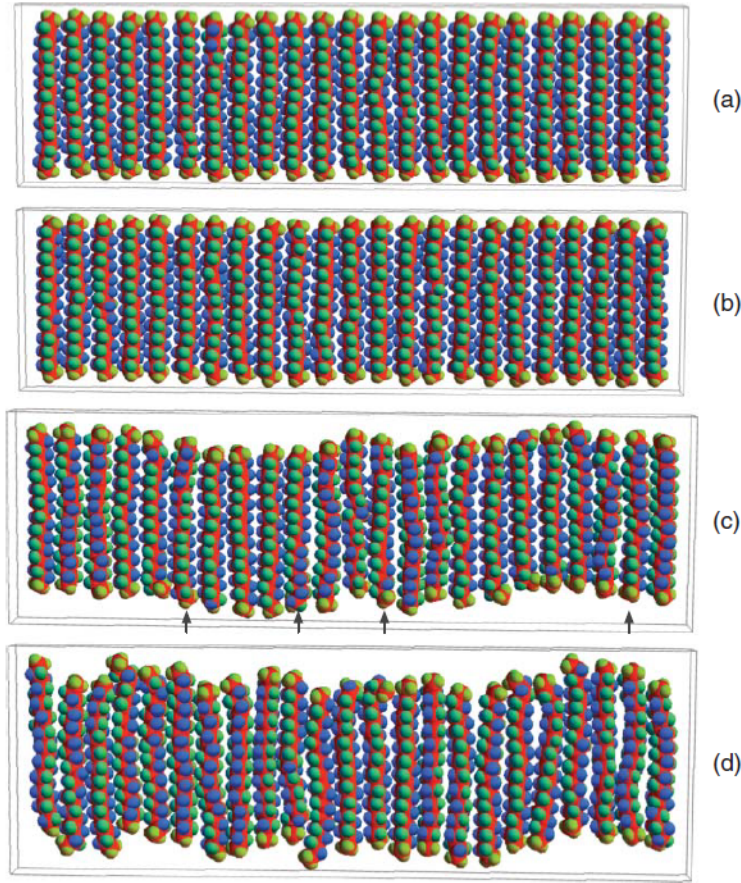


Figure 6: Snapshots of single row of molecules

(a) Orthorhombic, (b) Monoclinic, (c) R_I and (d) R_{II} phases. Alternating hydrogen have been colored green and blue to highlight the twisting.

3 Coarse-Grain Model

3.1 Introduction

The particle-based simulation is always limited by the number of interaction sites (or the degrees of freedom) constituting the system of interest. It is because the computation for the force (or energy) normally involves the calculation of the distance between each pair of the constituents. Such calculation needs to traverse all the possible pairs in the system while the number of pairs (N) is scaling in the fashion of N^2 . Therefore, the required computation time also scales accordingly.

To overcome this bottleneck, a simulation therefore needs a systematic approach that reduces the number of interaction sites (or the degree of freedom) while still maintaining the chemical, physical properties to some extent. Such approach is also called Coarse-grain model (CG). Taking an atomic system as example, instead of calculating atoms each by each, CG treats the constituting sites as 'a lump' of atoms. That is, some atoms are incorporated together and are treated as a whole. The internal degree of freedom is omitted and some information is thus missing. However, the computation efficiency is enhanced. Therefore a trade-off always exists between the large-scale computation efficiency and the detailed information.

3.2 Design Force-Field for Coarse-Grain Model

Since CG lumps atoms together as an entity, a force-field, or potential, to describe the interaction must be sufficient to describe the new constituent with satisfied resulting properties. The potential for CG had been parameterized with respect to microscopic level obtained from simulation of a fine-grained

All-atoms	United-atoms	United-monomers
OPLS-AA [11] DREIDING [14]	MARTINI [12] RR [15] CG2 [17] TraPPE-UA [18] DR [19]	CG-PVA [13] TraPPE-CG [16]

Table 2: List of three categories of CG model resolution and their corresponding force-field

model, or to experimental data. There are roughly three ways to obtain a good CG potential as follow.

- First approach for CG potential is the iterative Boltzmann inversion procedure (IBI). IBI first matches the radial distribution function(RDF) for a CG model to the corresponding RDF obtained from an atomic simulation or an experimental data (such as X-ray scattering data). Afterword, the potential is tabulated and fit to match RDF. The equation is shown below,

$$RDF(r) = e^{-\frac{U(r)}{k_B T}} \quad (1)$$

- Second approach is to match the forces (described by a linear combination of terms) acting on the CG model to the forces observed during individual configuration of a trajectory for the fine-grain model. This approach relies on microscopic information and so it is not fitted to the ensemble average properties such as RDF. By the integrating the force equation below, the potential will be obtained.

$$F(r) = -\frac{\partial U(r)}{\partial r} \quad (2)$$

- Third approach is like the same way as standard all-atoms force-field. It usually uses the analytic potential such as spring-like potential, Morse potential, LJ 12-6 potential to fit to thermodynamic data.

Normally, many CG models will not just singly adapt one of the approach, but they hybridize all the approaches based on the system of interest. For example, Shelly et al. [10] developed a hybrid model for phospholipids where water and alkane parameters are fitted to the bulk density by analytic potential, and the other parameters are determined by the IBI.

3.3 Different Coarse-Grain Model

CG model ‘lumps’ atoms into a bead and treat the bead as an entity. Therefore, depending on the size of beads, the information could be detailed or rough. Normally, it is called the ‘resolution’ of the simulation. When the level of resolution is lower, more atoms are incorporated into the bead. However, less information will be known since some of the inter-atomic interactions are omitted. In the contrary, when the level of resolution is higher, less atoms are incorporated into the beads. More information is available. In a word, normally, the level of resolution decides the outcome and time required for the simulation.

There are all levels of resolution, here only three representative levels and their corresponding CG force-fields are listed. They are All-atoms, United-atoms, and United-monomers respectively. They are shown in Figure 7. The All-atoms model is the atomic force-field, which means the basic unit is atom and therefore the resolution is only higher than electronic level. This model is only listed for the comparison. United-atoms model, as indicate by its name, it treats atoms together as bead. For example, normally, the $-CH_2-$ repeating unit in hydrocarbon is treated as one bead called CH_2 . As for the United-monomers model, for example, it could treat $-CH_2-CH_2-CH_2-$ as a bead called CCC_M . Table-2 below collects all the corresponding force-field for each level of coarse-grain resolution.

A correct selection of different CG model is necessary before diving into any simulation. There is no definite rules for the selection and it all depends on the system of interest. For example, if the system is under biological environment, the MARTINI force-field is the choice since it is optimized to the physiological condition. Or if the vapor pressure is the focus, the TraPPE force-field is recommended since it is optimized to fit the liquid-vapor coexistent curve by Monte Carlo method.

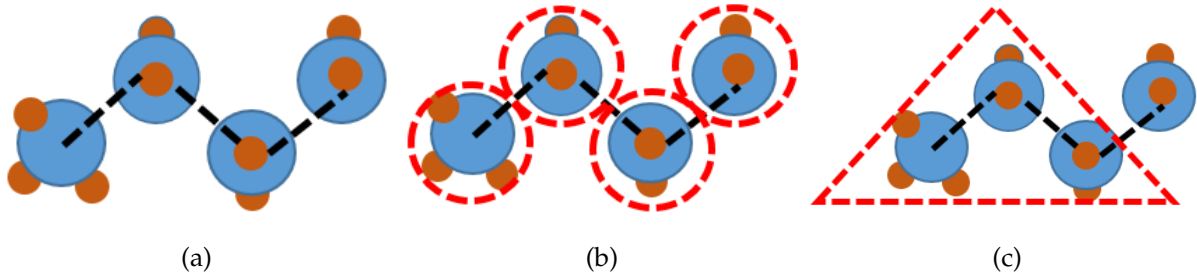


Figure 7: Schematic figure of different CG resolution

The coarse graining is higher from left to right and they are: (a) All-atoms (b) United-atoms (c) United-monomers model

C_n	T	Exp.	RR	CG-PVA	CG2
C_{10}	T_c	243	~ 235	~ 180	~ 460
	T_m	243	~ 300	~ 250	>600
C_{20}	T_c	310	~ 315	~ 230	~ 490
	T_m	310	~ 380	~ 280	>600
C_{30}	T_c	355	~ 325	N/A	N/A
	T_m	355	~ 410		

Table 3: Direct cooling/ heating simulation result

The simulation results for the crystallization temperature (T_c) and melting temperature (T_m) of three different length of N-alkanes by direct cooling/ heating method: experimental result, RR, CG2 and CG-PVA

3.4 Preliminary Screening of Coarse-Grain Models

This project is focusing on the CG simulation of crystallization of N-alkane, so the system of interest is under a larger-scale interaction of hydrocarbon. All-atoms model for similar system has been studied and it could already well-produce the crystallization process. Though due to the concern of calculation efficiency and the target information, it will not be considered in this project. As for the MARTINI force-field, which uses shifted LJ (12-6) potential, is designed for the use of biomolecular simulation of lipids, surfactants and proteins. The force-field parameters are fitted to reproduce the free energy of vaporization, hydration, and partitioning between water and organic phases at 300K. The temperature range of interest will be larger and the system is water free. In other words, the MARTINI force-field will not be a suitable one since the system of interest is not an aqueous one. The fitting between water and organic molecule will perhaps even distract the result instead.

To choose the best one from the rest of force-fields (RR, DR, CG2, CG-PVA, ,TraPPE-UA, TraPPE-CG), here we first select three of them to compare, that is RR, CG2 and CG-PVA. According to the research by C. Luo et al. [15] The tested system contains 200 molecules (6000 beads for RR, CG and 3000 beads for CG-PVA model). The system are first relaxed at 600K for 10 ns and then continuously quench to 200K at a cooling rate 10 K/ns followed by a annealing at 600K at the same heating rate. Their melting temperature (T_m) and crystallization temperature (T_c) are obtained by such direct cooling/ heating method and are listed as Table-3.

From table-3, given crystallization temperature (T_c), the result from RR model is the closest one to the experimental data; given the melting temperature, the result from CG-PVA model is the closest one. In the project, the focus is on the crystallization of N-alkane from its melt and so the crystallization temperature is considered. Besides the temperature, as paper [15] points out, RR model is the only one, among CG-PVA and CG2, capable to produce two phases of N-alkane crystal (triclinic/orthorhombic and rotator phase). It shows that CG2 and CG-PVA are not of consideration.

The comparison for the rest is still unknown. However, since the resolution of TraPPE-CG, which is three monomer-based model, is lower than the resolution of CG-PVA, which is two monomer-based model, the result of TraPPE-CG will be more deviated from the one from CG-PVA model. Apparently, TraPPE-CG may not be of consideration. So far, the remaining models are RR, DR and TraPPE-UA. In this project, a comparison will be made in order to choose the best one based on the simulation of T_c ,

T_m , and liquid density.

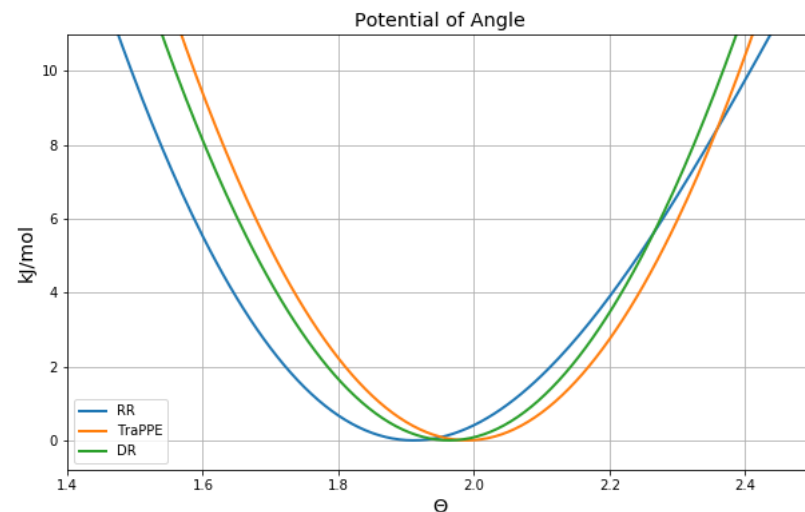
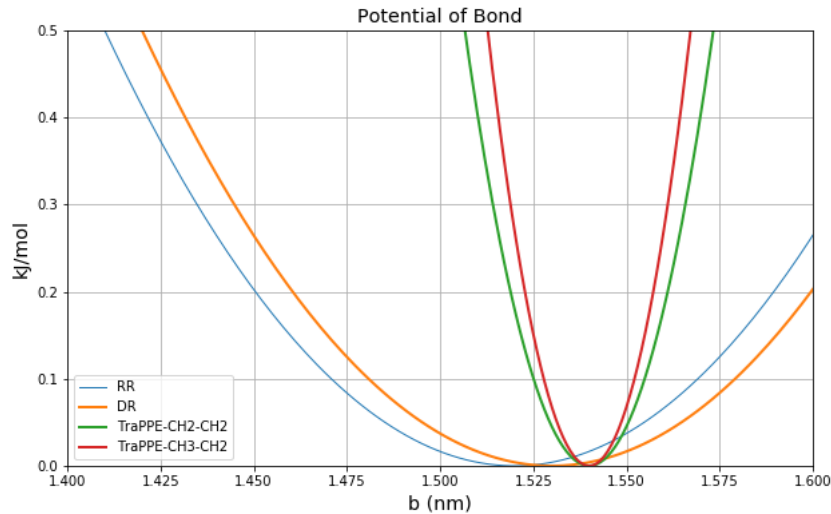
4 Details of Selected Coarse-Grain Models

4.1 Coarse-Grain Model Parameters

In this section, the selected CG models (RR, DR and TraPPE respectively) are compared based on their differences between mathematical form of potential. CG model normally comprises of two categories. Bonded (also called short-range) interaction and Non-bonded (also called long-range) interaction. Bonded interaction can be further decoupled into bond interaction (1-2 or 2 body) interaction, angle (1-2-3 or 3 body) interaction and dihedral (1-2-3-4 or 4 body) interaction; Non-bonded interaction includes Lennard Jones interaction and Coulomb interaction. Thus CG model can be represented as below and each contribution may take different mathematical formulas. All the detailed parameters for selected CG models are listed in Table-4.

$$U_{CG} = U_{bonded} + U_{non-bonded} \quad (3)$$

$$= \{U_{bond} + U_{angle} + U_{dihedral}\} + \{U_{LJ} + U_{Coulomb}\} \quad (4)$$



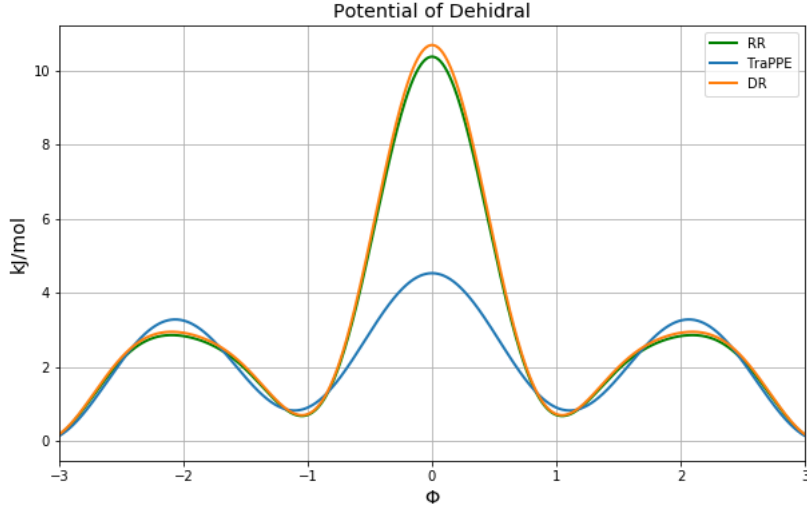


Figure 8: Plot of CG potential

The figures listed from top to bottom are the plots of bond, angle and dihedral potentials respectively

These potential details are quite straightforward in Table-4. However, to have a clear picture in mind, the respective potentials are plotted for comparison as indicated by Figure-8. First, the potential of bond for RR is similar to the one for DR while TraPPE-UA is relatively rigid as the curvature for TraPPE-UA is larger than the rest. Because TraPPE-UA treats $-CH_3-$ and $-CH_2-$ differently in bond interaction, there are two functions to describe different bond interactions (green and red line). Second, the potentials of angle for all are similar. Third, As for the dihedral potential, all of them are fitted according to the same method based on dihedral interaction of butane [20]. It can be told from Figure-8. TraPPE-UA and DR have largest peak in the middle ($\Phi \approx 0$). Therefore, as shown by Figure-9, by the LAMMPS definition of dihedral angle (Φ), TraPPE-UA and DR are less likely to have a coil conformation but more likely to have a stick-like conformation.

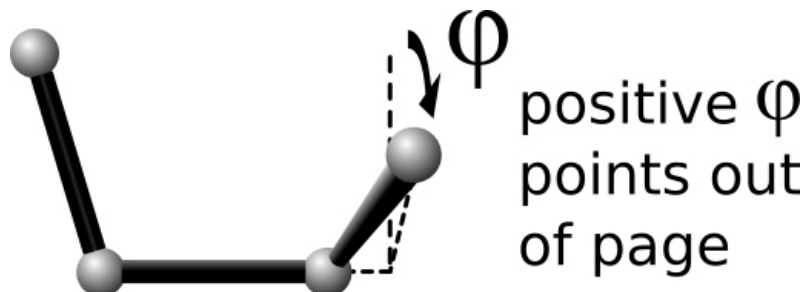


Figure 9: LAMMPS definition of dihedral angle Φ

As mentioned previously, Non-bonded interactions include Lennard-Jones and Coulomb interaction interactions. Given the target molecule (Octacosane), there is only saturated carbon, which is sp^3 hybridization so it is electrically inert. Thus, Coulomb interaction will not be considered. Figure-10 shows the Lennard-Jones interactions (in reduced unit) for three CG models. Again, since DR and TraPPE-UA treat $-CH_3-$ and $-CH_2-$ differently in Lennard-Jones interactions, there are five functions in Figure-10. TraPPE-UA has the strongest $-CH_3-$ interaction and the weakest $-CH_2-$ interaction. To sum up, among the selected CG models, RR is the most simple one which only one bead type exists while TraPPE-UA pronounces distinguishes two bead types for most interactions. In the following sections, in order to assess the selected CG models, a few properties are tested and compared.

Form of Potential	RR	DR	TraPPE
Mass	$m_{CH2} = 14.09 \text{ amu}$ $m_{CH3} = 15.04 \text{ amu}$	$m_{CH2} = 14.02 \text{ amu}$ $m_{CH3} = 15.04 \text{ amu}$	$m_{CH2} = 14.02 \text{ amu}$ $m_{CH3} = 15.04 \text{ amu}$
Bond $U_{bond} = k_1(b - b_0)^2$	$k_1 = 41.348 \text{ kcal \AA}^{-2} \text{ mol}^{-1}$ $b_0 = 1.52 \text{ \AA}$ (fixed bond length)	$k_1 = 41.348 \text{ kcal \AA}^{-2} \text{ mol}^{-1}$ $b_0 = 1.53 \text{ \AA}$ (fixed bond length)	$k_{CH3-CH2} = 674.600 \text{ kcal \AA}^{-2} \text{ mol}^{-1}$ $k_{CH2-CH2} = 450.000 \text{ kcal \AA}^{-2} \text{ mol}^{-1}$ $b_{CH3-CH2} = 1.540 \text{ \AA}$ $b_{CH2-CH2} = 1.540 \text{ \AA}$ (fixed bond length)
Angle	$k_2 = 59.751 \text{ kcal mol}^{-1}$ $\theta_0 = 109.471^\circ$	$k_2 = 62.141 \text{ kcal mol}^{-1}$ $\theta_0 = 112.50^\circ$	$k_{CH3-CH2} = 62.100 \text{ kcal mol}^{-1} \text{ rad}^{-2}$ $k_{CH2-CH2} = 62.100 \text{ kcal mol}^{-1} \text{ rad}^{-2}$ $\theta_{CH3-CH2} = 114.00^\circ$ $\theta_{CH2-CH2} = 114.00^\circ$
Dihedral	$k_3 = 2.151 \text{ kcal mol}^{-1}$ $a_0 = 1$ $a_1 = -1.3100$ $a_2 = -1.4140$ $a_3 = 0.3297$ $a_4 = 2.8280$ $a_5 = 3.3943$	$k_3 = 2.217 \text{ kcal mol}^{-1}$ $a_0 = 1$ $a_1 = -1.3100$ $a_2 = -1.4139$ $a_3 = 0.3296$ $a_4 = 2.8279$ $a_5 = 3.3910$ (shifted to match LAMMPS defined Φ)	$k_3 = 0.5 \text{ kcal mol}^{-1}$ $a_0 = 0$ $a_1 = 1.4110$ $a_2 = -0.2710$ $a_3 = 3.1450$
Lennard-Jones $4\epsilon \left[\left(\frac{\sigma}{r} \right)^{12} - \left(\frac{\sigma}{r} \right)^6 \right]$	$\epsilon = 0.119 \text{ kcal mol}^{-1}$ $\sigma = 3.8 \text{ \AA}$ $R_c = 9.5 \text{ \AA}$	$\epsilon_{CH2} = 0.143 \text{ kcal mol}^{-1}$ $\epsilon_{CH3} = 0.153 \text{ kcal mol}^{-1}$ $\sigma_{CH2} = 3.923 \text{ \AA}$ $\sigma_{CH3} = 3.740 \text{ \AA}$ $R_c = 15 \text{ \AA}$ (use geometric mixing rule when $i \neq j$)	$\epsilon_{CH2} = 0.097 \text{ kcal mol}^{-1}$ $\epsilon_{CH3} = 0.194 \text{ kcal mol}^{-1}$ $\sigma_{CH2} = 3.950 \text{ \AA}$ $\sigma_{CH3} = 3.750 \text{ \AA}$ $R_c = 14. \text{ \AA}$ (use geometric mixing rule when $i \neq j$)

Table 4: Details of potential RR, DR & TraPPE

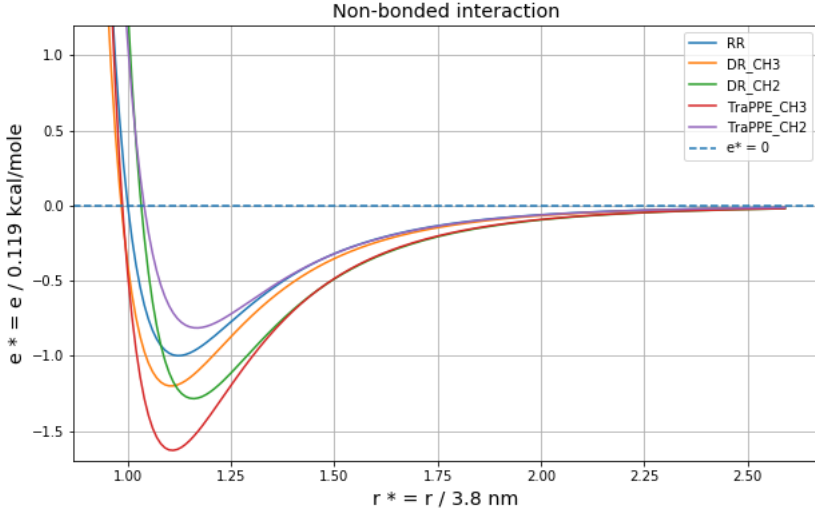


Figure 10: Lennard-Jones potential

4.2 Liquid Density Simulation

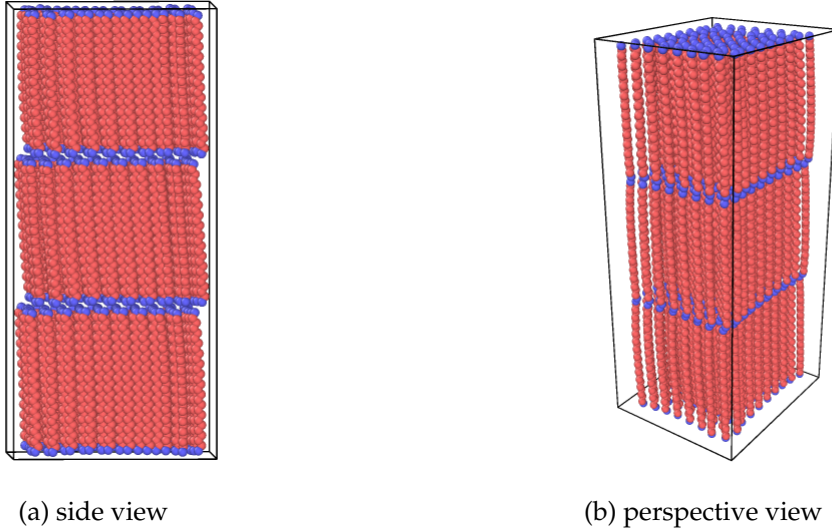


Figure 11: Input structure for the liquid density simulation

The red bead and blue beads represent $-CH_3-$ and $-CH_2-$ monomers

- **Method:**

In order to test the fidelity of the selected CG models, liquid density is first tested. The whole simulation is under periodic boundary condition and the initial structure is a pseudo-crystal made of 200 Octacosane molecules in a $30 \times 30 \times 90 \text{ \AA}^3$ box as shown by Figure-11. The iterative style is Verlet and the time-step, temperature coupling time, pressure coupling time are 1 fs, 100 fs and 1000 fs respectively. After the geometry optimization, the system is heated to 800K, 1 atm for 0.5 ns to ensure that it restores the amorphous state, then it is quenched to target temperatures ($T \in \{373.15K, 398.15K, 423.15K, 448.15K, 473.15K, 498.15K, 523.15K, 548.15K\}$), 1 atm and relaxes for 4ns.

- **Results and Discussion:**

The simulation result is shown in Figure-12. It can be easily noticed that TraPPE-UA (red line) has the closest values to the experimental data [21] (purple line) while DR has the worst result (green line). For example, when $T = 398.15K$, the relative error of density for RR, DR and TraPPE are 9.9%, 15.09% and 0.65%. Therefore, for convenience, only RR and TraPPE-UA will be studied later on.

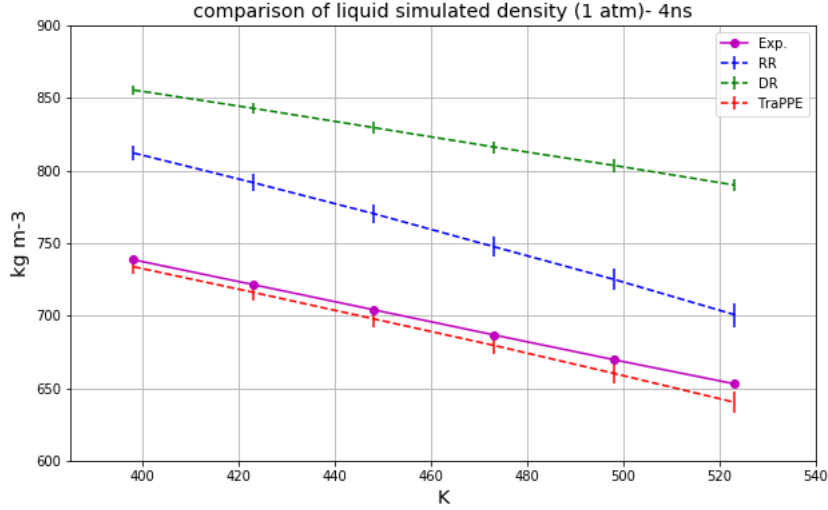


Figure 12: Liquid density simulation result for selected CG models

4.3 Melting Point Simulation

4.3.1 Direct Heating/ Cooling Method

Other than liquid density, melting temperature (T_m) and crystallization temperature (T_c) are another parameter for the fidelity assessment of CG models. When the physical scale is large enough, the T_m and T_c are the same, which are also called solid-liquid transition temperature. The easiest way to get T_m/ T_c is by direct heating/ cooling method. It is done by gradually heating/ cooling the sample which is solid/ liquid. Afterwards, T_m/ T_c can be captured when there is a kink in enthalpy due to the release/ absorption of latent heat.

- **Method:**

Similarly, continued from the last section (liquid density simulation), the whole simulation is under periodic boundary condition and the initial structure is a pseudo-crystal made of 200 Octacosane molecules in a $30 \times 30 \times 90\text{\AA}^3$ box. Verlet iterative style is used. The time-step, temperature coupling time, pressure coupling time are 1 fs, 100 fs and 1000 fs respectively. While after geometry optimization, the crystal is kept at 300K for 0.5 ns and subsequently change temperature to 500K. The system is then kept at 500K for 0.5 ns and then cooled back to 300K with the chose cooling rate (10K/ns and 5K/ns).

- **Result and Discussion:**

The simulation result by direct heating/ cooling method for RR, is shown as Figure-14. Rows on left side are the result during heating process; the others are during cooling process. By simple observation, a clear kink can be noticed at around 1 ns for heating process and at around 2.7 ns for cooling process. The transition temperature, which is the temperature when the kink happened, can be captured. They are $T_m = 400K$ and $T_c = 270K$ respectively. Therefore, the upper bound and lower bound for the transition temperature, also called transition temperature window, is obtained, $T \in (400K, 270K)$. Although the experimental transition temperature, which is $T =$

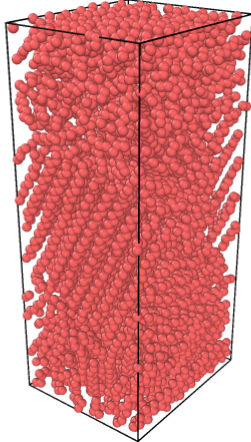


Figure 13: Final crystal structure from cooling process

A multi-crystal is shown. In the middle, the crystal is roughly oriented toward [101] direction; At the bottom, the crystal is roughly oriented toward [011] direction (it is not clear in the Figure).

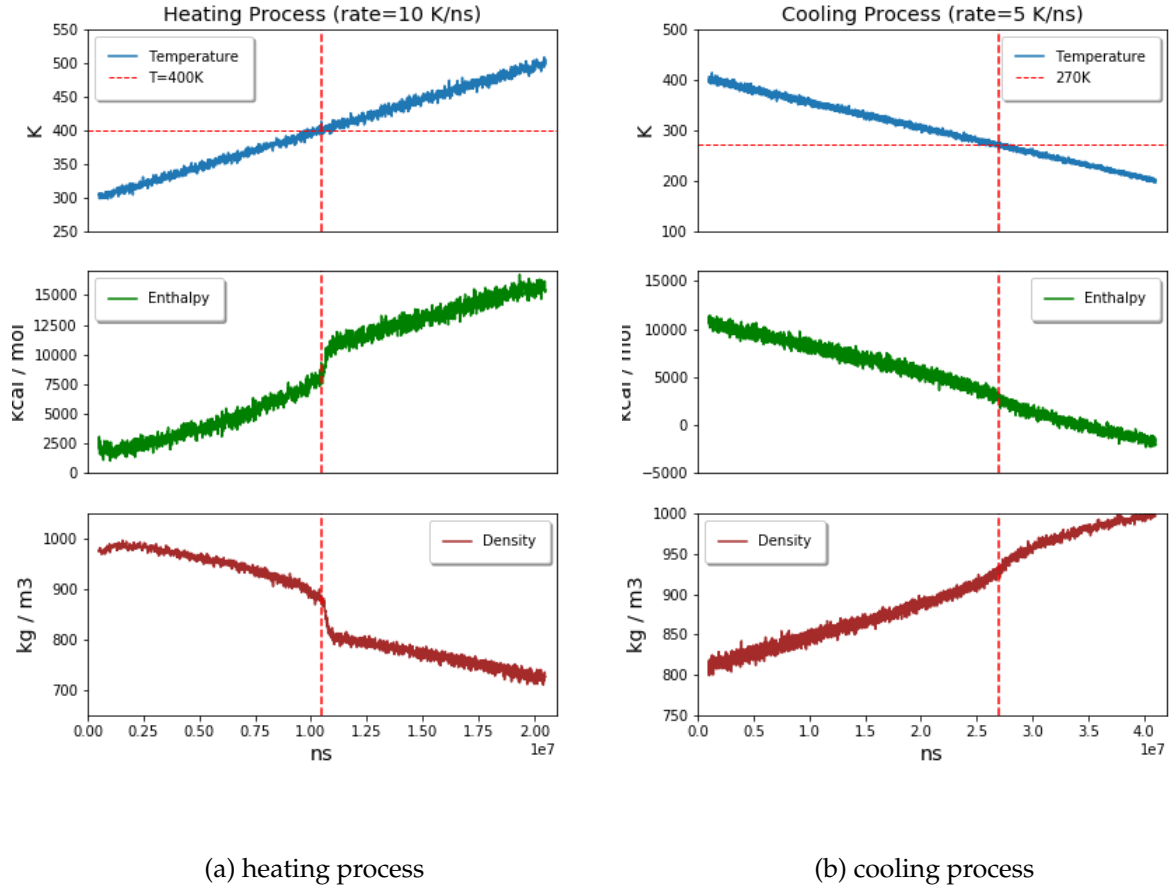
$337.5K$, is located in between transition temperature window obtained, the relative error is still quite large. In Figure-14-(b), the kink is not so obvious as one in Figure-14-(a). The reason comes from the effect of crystal size. The final crystal structure of cooling process is shown in Figure-13. As Figure-13 shows, it is poly-crystalline instead of a single crystal as initial crystal structure. The change of latent heat comes from the ordering of octacosane molecules. Due to poly-crystalline crystal, the extent of enthalpy change from crystallization is smaller compared to the change from melting. Therefore, the kink during cooling is not as large as one during heating. In direct heating/ melting method, the transition temperature window largely depends on the heating/ cooling rate and the finite size effect because the melting/ crystallization is a dynamic process. Given cooling process, if cooling rate (or the extent of under-cooling) is very large, all the molecules will be 'frozen' before they are able to arrange themselves into a equilibrium crystal structure and are kept at amorphous state. On the other hand, if the cooling rate is very small, the molecules will have enough time to arrange themselves. Thus, the smaller the cooling/ heating rate will result in a smaller, more accurate transition temperature window. It means the upper and lower bound of transition temperature window will converge toward a single value as the heating/ cooling rate becomes larger. However, it means a longer simulation time is required and an incredibly long simulation will be impractical. To sum up, the direct heating/ cooling method is very prone to the chosen heating/ cooling rate.

4.3.2 NPH Simulation

From last section it is understood that the direct heating/ cooling method is not always convenient since the transition temperature window depends on the heating/ cooling rate, which requires one to take efforts to tune to reasonable values. In order to have a easier, less time-consuming method, the NPH simulation is introduced to study the T_m and T_c . NPH simulation [22], namely, is a technique using ensemble constraint which holds the number of constituents, pressure and enthalpy as constant during the simulation. Figure-15 is a typical pressure(P)-enthalpy(H) phase diagram for water. As shown in the figure, When the pressure is fixed, there is a range of enthalpy where soild and liquid are in equilibrium. When the solid and liquid coexist, the temperature $T = T_m$ or T_c . Therefore, compared with direct heating/ cooling method, which tries to search the equilibrium 'point' (0-D) in P-T pahse diagram, the NPH simulation is more efficient because it is searching the equilibrium 'range' (1-D) in P-H phase diagram.

- **Method:**

For the simulation set up, the initial configuration is shown as Figure-16, which is containing a



(a) heating process

(b) cooling process

Figure 14: Simulation result of direct (a)heating/ (b)cooling method for RR

From top to bottom, each rows correspond to temperature, enthalpy and density, and the heating rate is 10 K/ns ; the cooling rate is -5 K/ns . The transition temperature window is obtained, $T \in (270\text{ K}, 400\text{ K})$, which is indicated by horizontal dashed line.

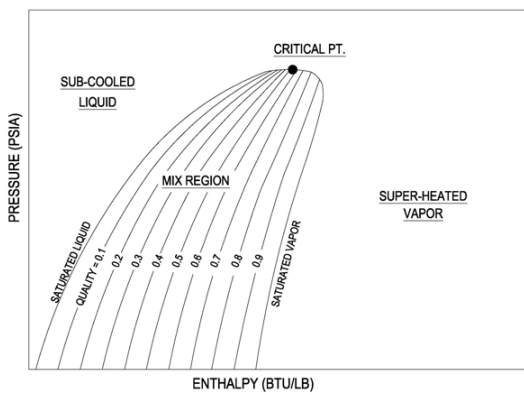


Figure 15: Typical P-H diagram of water

crystal (160 octacosane molecules) inside the liquid (640 octacosane molecules) in a $52 \times 171 \times 68 \text{\AA}^3$ box. The time-step, temperature coupling time, pressure coupling time are 1 fs, 200 fs and 2000 fs respectively. Verlet iterative style is used. The system is first subject to NPT ensemble to pump certain energy into the system for 0.05 ns ($T \in \{300, 325, 350, 375, 400, 425, 450, 475 K\}$). Then, the system is fixed under NPH ensemble and let the system evolves for 6 ns.

- **Result and Discussion:**

The NPH simulation result for RR and TraPPE-UA are shown in Figure-17 and Figure-18 respectively, each points correspond to one independent simulation which reaches the final equilibrium temperature and enthalpy. The transition temperature window lies between the right end of solid equilibrium curve (left-sided) and the left end of liquid equilibrium curve (right-sided). For RR, the transition temperature window is $T \in (356K, 357K)$ and the mean melting point $T_m = 356.5K$; For TraPPE-UA, the transition temperature window is $T \in (335K, 336K)$ and the mean melting point $T_m = 333.5K$. Compared with direct heating/ cooling method, the result from NPH simulation is far more accurate and precise that the transition temperature window is only 1K wide and the relative error of mean melting temperature is 5.63% and 1.18%.

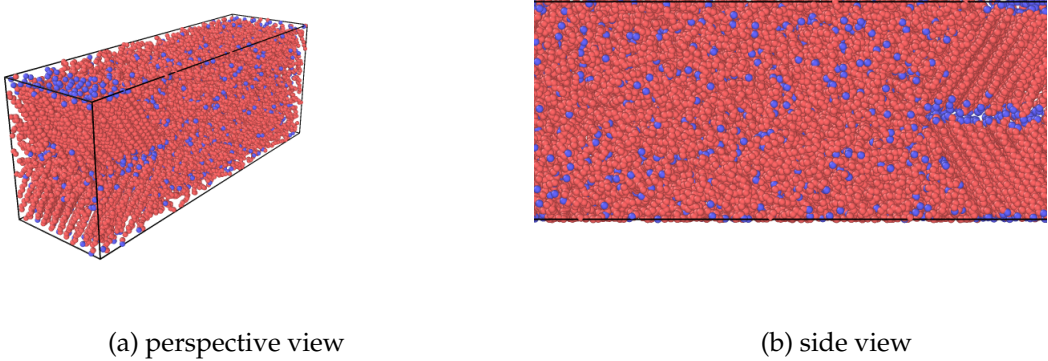


Figure 16: Input structure for the NPH simulation

The red bead and blue beads represent $-CH_2-$ and $-CH_3-$ monomers; (b) the right side of box is in solid state and the rest is in liquid state. The figure-(b) is flipped of figure-(a).

4.4 CG models' Performance

As mentioned previously, the fidelity and efficiency are counterbalance concerning CG model. Aside from the properties like liquid density and melting point, the performance for all CG models should also be tested in order to pick the best suited CG model.

- **Method:**

In this section, a series of loop time tests for RR and TrapPE-UA for different number of octacosane molecules are done. All the simulation are under NPT ensemble. The whole simulation is under periodic boundary condition. Similar to structure shown as Figure-11, the initial structure is a pseudo-crystal made of N Octacosane molecules ($N \in \{40, 400, 2000, 4000\}$) in a $50 \times 900 \times 70 \text{\AA}^3$ box. The iterative style is Verlet and the time-step, temperature coupling time, pressure coupling time are 1 fs, 100 fs and 1000 fs respectively. After the geometry optimization, the system is heated to 800K, 1 atm for 1000 steps and the average calculation time per step is recorded for samples with different N Octacosane molecules.

- **Result and Discussion:**

Here the property performance (P) is define as below,

$$P \equiv \frac{\text{iteration}}{\text{second}} \quad (5)$$

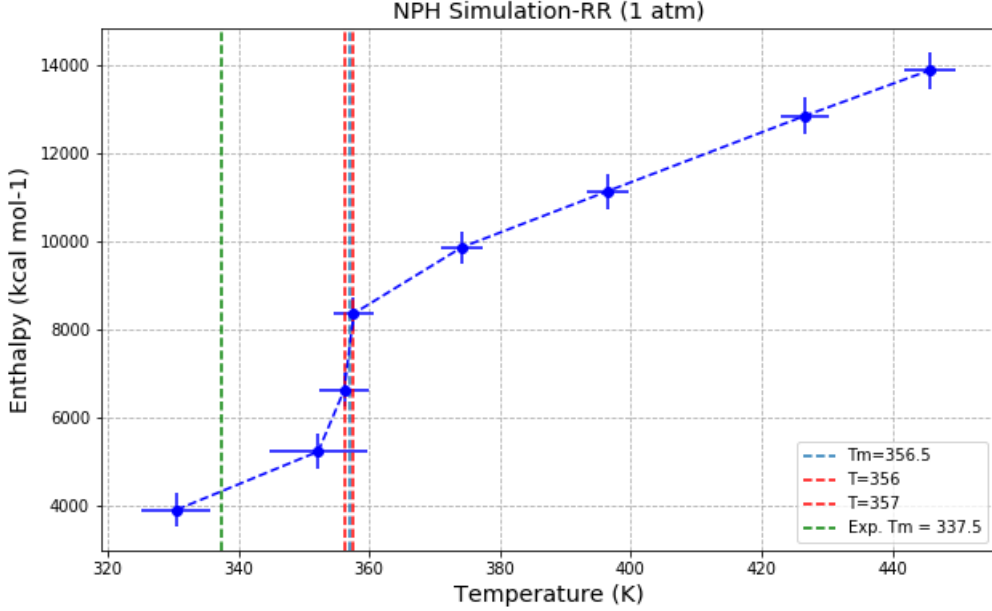


Figure 17: NPH simulation result for RR

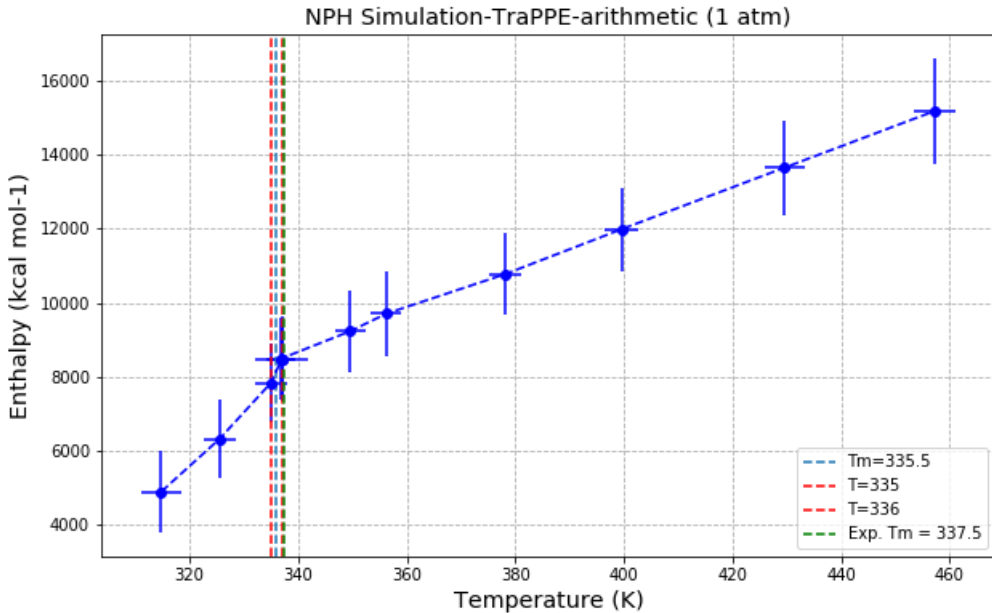


Figure 18: NPH simulation result for TraPPE-UA

The simulation result is shown in Figure-19. The fitting curves for both are as below,

$$\log_{10}(P_{RR}) = -1.18 \times \log_{10}(N) + 4.49 \quad (6)$$

$$\log_{10}(P_{TraPPE-UA}) = -1.19 \times \log_{10}(N) + 4.30 \quad (7)$$

As fitting curves show, the performance decreases linearly with number of molecules and both functions are close to parallel. For number of molecules lower than $N = 10^{3.602} \approx 4000$, TraPPE-UA is around $10^{0.19} = 1.54$ times slower than RR. The reason that two CG models with mainly

Properties CG models	Liquid Density	Melting Point	Performance
-	$\Delta\rho_{liq}/\rho_{liq,exp}(398.5K)$	$\Delta T_m/T_{m,exp}$	$\log(P)$
RR	9.90%	5.63%	$-1.18 \times \log(N) + 4.49$
TraPPE-UA	0.65%	1.18%	$-1.19 \times \log(N) + 4.30$

Table 5: Table of comparison between RR and TraPPE-UA

changing in parameters for the same types of energy terms differs 1.5 times in runtime lies in their cutoffs. There are plenty of optimization in LAMMPS. For example, the particle will have its neighbor-list, which is updated a few steps after or each step. During the force/ energy calculation, instead of looking for all the particles, it looks at the particles in the neighbor list. Therefore, how often the neighbor list is constructed and the size of neighbor list will decide the calculation time. For RR and TraPPE-UA, their cutoffs are 9.5 Å and 14 Å respectively. The ratio of volume for neighbor list is $14^3/9.5^3 \approx 3.2$, which mainly contributes to the difference in runtime.

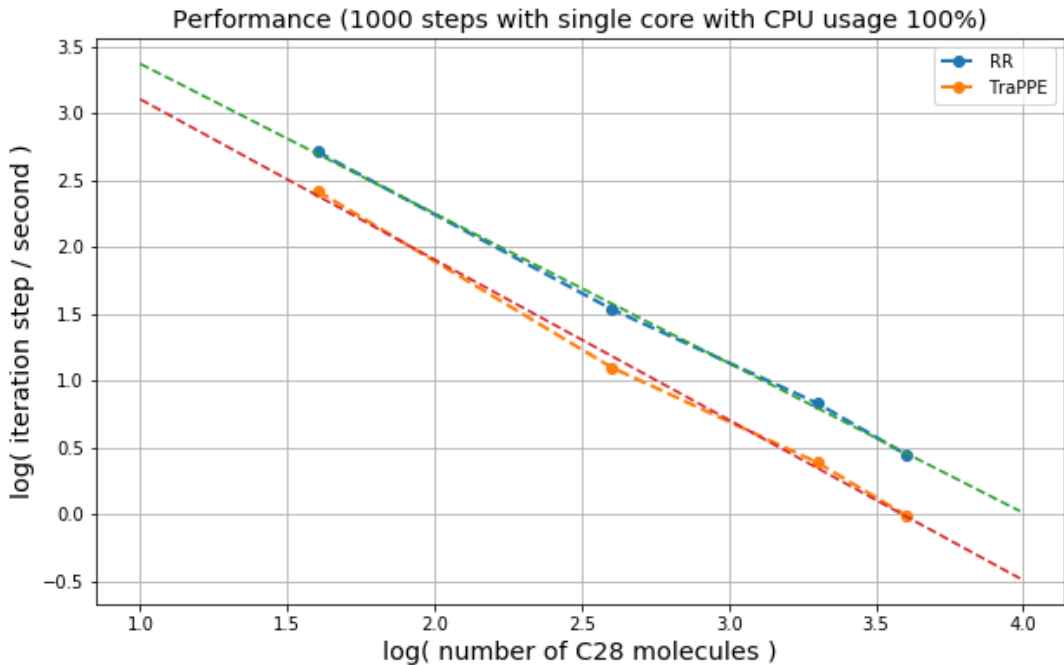


Figure 19: Performance (P) vs Number of molecule (N) for RR and TraPPE-UA

4.5 Selection of CG models

From previous sections, a few properties are calculated and compared between two CG models (RR and TraPPE-UA), including liquid density, melting point and performance. These information are listed in Table-5. First, from liquid density simulation result, TraPPE-UA performs a lot better (relative error= 0.65%) than RR while RR still performs quite well (relative error= 9.9%). Second, by NPH simulation instead of direct heating/ cooling method, the resulting melting temperature from TraPPE-UA (333.5 K) is also closer to experimental result (337.5 K) than melting temperature does from RR (356.5 K). Third, although TraPPE-UA out-performs RR in predicting both liquid density and melting point, the performance of TraPPE-UA is roughly 1.5 times slower than RR. Combining all, RR will have a better calculation efficiency (around 5.5 times faster when $N = 10^4$) when number of molecules is ‘really large’ ($N \geq 10^4$). However, the prediction error will be bigger as well. On the other hand, if the number of

molecule is medium ($N \leq 10^4$), TraPPE-UA is a better choice due to a more precise and accurate prediction. Still, as the name entailed, TraPPE-UA is transferrable which means this CG model is fitted to a range of elements. If a cross-element system such as system includes H, C, O, N , TraPPE-UA will be a good choice. In this project, the number of molecules is medium (around a few thousand of octacosane at most). Therefore, TraPPE-UA is chosen as the main CG model throughout the project later on.

5 Study of Crystal Growth

From previous section, a suitable CG model, TraPPE-UA, has been selected. In this section, the mechanism of crystal growth and the effect on crystal growth from introducing inhibitor will be investigated.

5.1 Averaged Local Bond Order Parameter (\overline{Q}_l)

All the studies in this section are based on "Averaged Local Bond Order Parameter, ALBO" (or so called averaged local order parameter, \overline{Q}_l) [23]. ALBO is one of common parameters to identify the local structure and to distinguish the structures of liquid (amorphous phase) and crystal (order phase). As such, before exploring anything, the principle of ALBO will first be explained here. ALBO originates from the local bond order parameter (q_{lm}), which is defined as below,

$$q_{lm}(i) = \frac{1}{N_b(i)} \sum_{j=1}^{N_b(i)} Y_{lm}(r_{ij}) \quad (8)$$

where $N_b(i)$ corresponds to the number of nearest neighbor of particle i and $Y_{lm}(r_{ij})$ are the spherical harmonics. This parameter (q_{lm}) is able to characterize the local positional structure by projection of the positions of a particle's neighbors onto spherical harmonics. Provided the q_{lm} value should be invariant under inversion, the value of l is restricted to even-l. In order to have a better contrast of q_{lm} between different local structures, q_{lm} is averaged over its neighbor spatially, $\widetilde{N}_b(i)$ (atoms including itself within cutoff). It is calculated as below,

$$\bar{q}_{lm}(i) = \frac{1}{\widetilde{N}_b(i)} \sum_{k=0}^{\widetilde{N}_b(i)} q_{lm}(k) \quad (9)$$

Because $\bar{q}_{lm}(i)$ for a given l can be scrambled drastically by changing to a rotated coordinate system, it is important to consider rotationally invariant, such that \overline{Q}_l is defined as below,

$$\overline{Q}_l(i) \equiv \sqrt{\frac{4\pi}{2l+1} \sum_{m=-l}^l |\bar{q}_{lm}(i)|^2} \quad (10)$$

From previous study [23], the choice of cutoff is usually set to $1.2r_0$ computationally, where r_0 is the minimum in a Lennard-Jones potential. For example, all reasonable definitions lead to \overline{Q}_l which vanish in isotropic liquids for $l > 0$ and which are nonzero in cubic solids for $l \leq 4$. In this project, in order to distinguish the state between amorphous and the crystalline structures for N-alkane, the cutoff is set to $1.4r_0$ and l is set to 6 (\overline{Q}_6) [8].

5.2 Rate of Crystal Growth

From section 4.3.2, it can be noticed that a crystal growth will happen when the equilibrium temperature is lower or equal to the melting temperature. In order to understand more details about it, in this section, the crystal growth is studied. In last section, it is shown that ALBO with $l = 6$ (\overline{Q}_6) is able to provide a means to identify the local structures between amorphous and crystalline structures for N-alkane system. By coloring all the particles based on their own \overline{Q}_6 , two clear regions for order and disorder can be noticed easily as shown by Figure-20(b), and the initial system is shown without coloring as Figure-20(a) shown.

- **Method:**

The simulation setup is the same as the one for section 4.3.2. There are five initial configurations,

which all are similar as Figure-16 containing a crystal (160 octacosane molecules) inside the liquid (640 octacosane molecules) in a $52 \times 171 \times 68\text{\AA}^3$ box. For each configuration, their crystal locates at different places (shifted along x-direction). The time-step, temperature coupling time, pressure coupling time are 1 fs, 200 fs and 2000 fs respectively. Verlet iterative style is used. First the velocities for each sample is randomized to ensure each sample is independent. Subsequently the system is subject to NPT ensemble for 0.01 ns ($T = 300K$). Then, the system is fixed under NPH ensemble and let the system evolves for 30 ns. For every 0.1 ns, \overline{Q}_6 calculation is calculated and recorded internally by LAMMPS. Finally, post-calculation of \overline{Q}_6 is done separately.

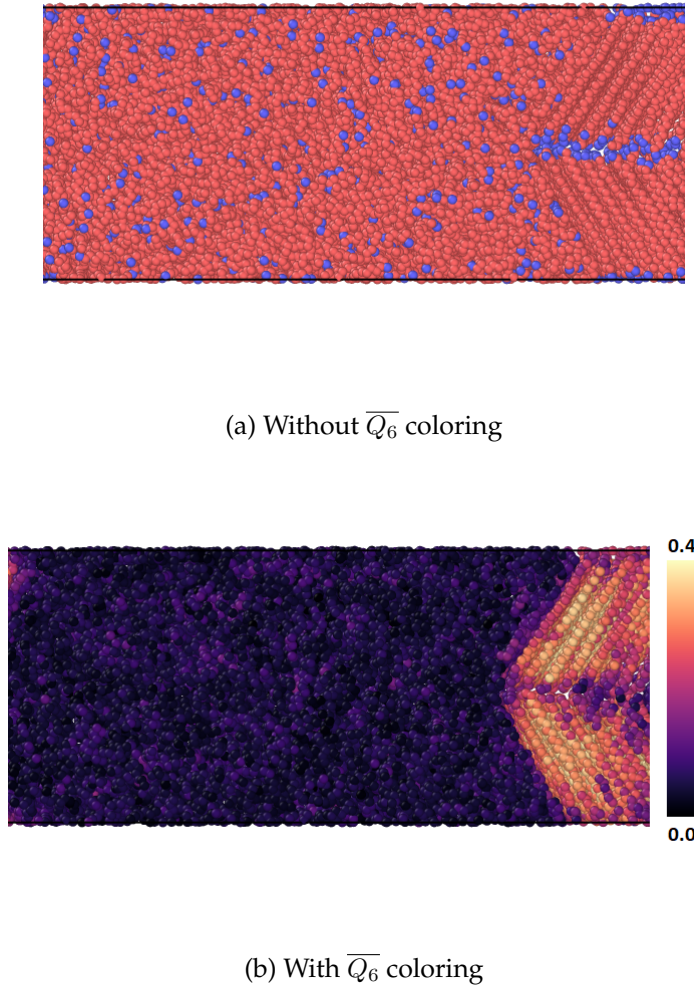


Figure 20: Initial structure for the crystal growth simulation at 0ns

Two clear regions for order and disorder can be found in Figure-(b); Color code: Figure-(a) The red bead and blue beads represent $-CH_2-$ and $-CH_3-$ monomers; Figure-(b) Light yellow and dark purple represent order and disorder ($\overline{Q}_6 \in [0.0, 0.4]$) respectively.

- **Result and Discussion:**

As shown by Figure-21, by \overline{Q}_6 coloring, the crystal growth can be observed as time passes (Figure-21 (a)-(d) are different snapshots from the system side-view). Starting from simple, here the rate is only considered in the x-direction (the horizontal direction in the Figure-21). To capture the rate of crystal growth, first the length of order and disorder should be identified. In order to do so, the crystallinity distribution along x-direction for different time is calculated. Along x-direction in

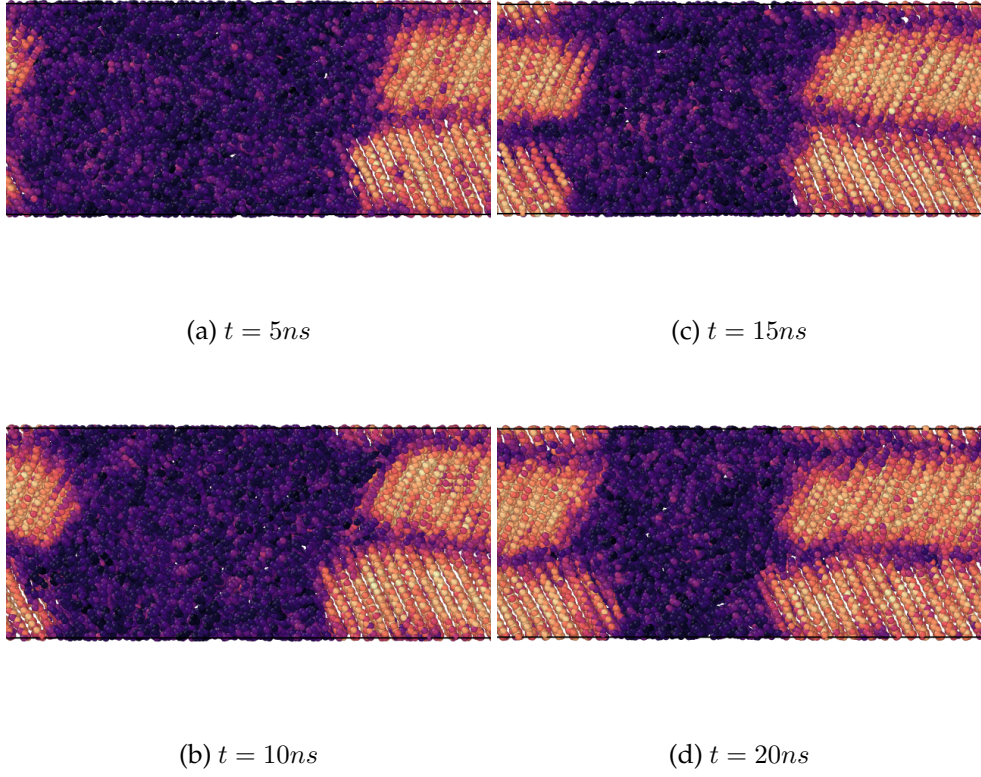


Figure 21: Time evolution of crystal growth

the simulation box, it is divided into 50 layers. For each layer, the crystallinity is calculated based on $\overline{Q_6}(i)$ value of each particle i . By observation, it is known $\overline{Q_6} \in [0.0, 0.4]$. From empirical test, $Q_6 = 0.2$ is sufficient enough to distinguish two states. Thus if $\overline{Q_6}(i) \geq 0.2$, particle i belongs to crystallized particle, otherwise it is non-crystallized. Therefore, the crystallinity of certain layer j $Xc(j)$ can be defined as the portion of crystallized particles $N_{crystallized}(j)$ (\forall particle i layer j , $\overline{Q_6}(i) \leq 0.2$) over the total particles $N_{total}(j)$ in that layer j ,

$$Xc(j) \equiv \frac{N_{crystallized}(j)}{N_{total}(j)} \quad (11)$$

Figure-22 shows a result of crystallinity distribution for different time ($t = 0, 5, 10, 15, 20\text{ns}$). Similarly, from the Figure-22 it can be observed that the crystal is growing. The boundaries between high and low Xc move toward both $+x$ and $-x$ direction respectively and the crystallinity of each layer converges when $Xc \approx 0.8$. Now the crystallinity distribution along x -direction for different time has already been calculated. In this project, the rate of crystal growth is defined as

$$rate \equiv \frac{\Delta l_c}{2\Delta t} \quad (12)$$

where l_c is the length of crystallized portion along x -direction. Along x -direction, a layer is counted as crystallized if $Xc(j) \geq 0.02$. Because there are two boundaries each moving in opposite direction, the rate should be divided by 2. The crystal length evolution for TraPPE and RR are shown as Figure-23 and Figure-24 for a few independent samples. Linear regression is calculated for each of them. Table-6 shows the rates of crystal growth for RR and TraPPE. It can be seen that the rate for RR ($\approx 15 \text{ cm/sec}$) is faster than the rate for TraPPE ($\approx 10 \text{ cm/sec}$) by around 1.5 times.

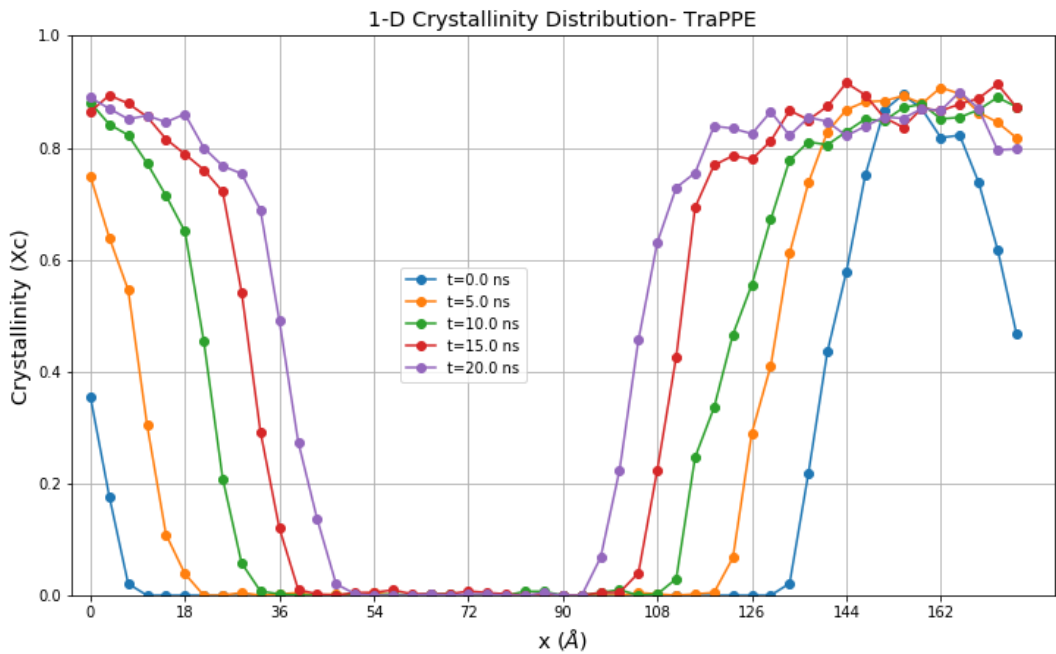


Figure 22: Crystallinity distribution along x-direction for different time

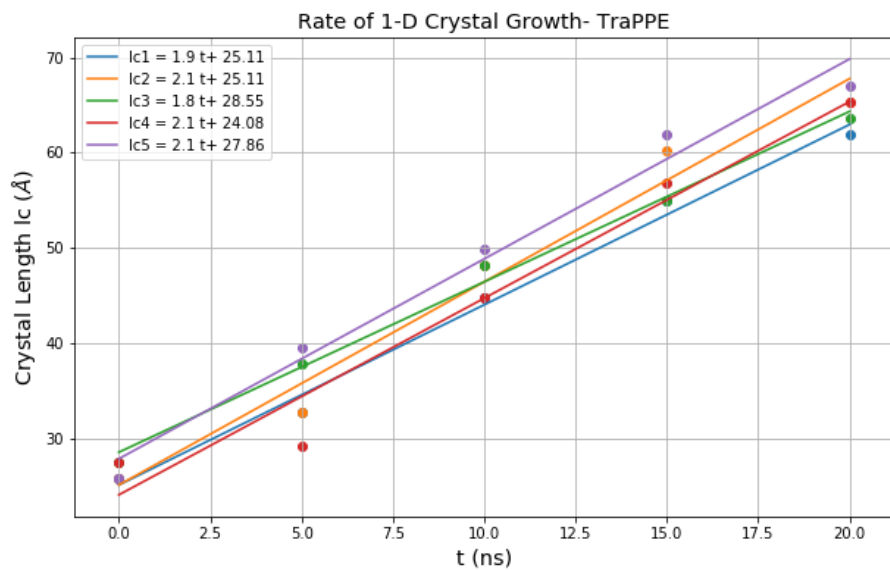


Figure 23: Crystal length evolution vs. time for TraPPE

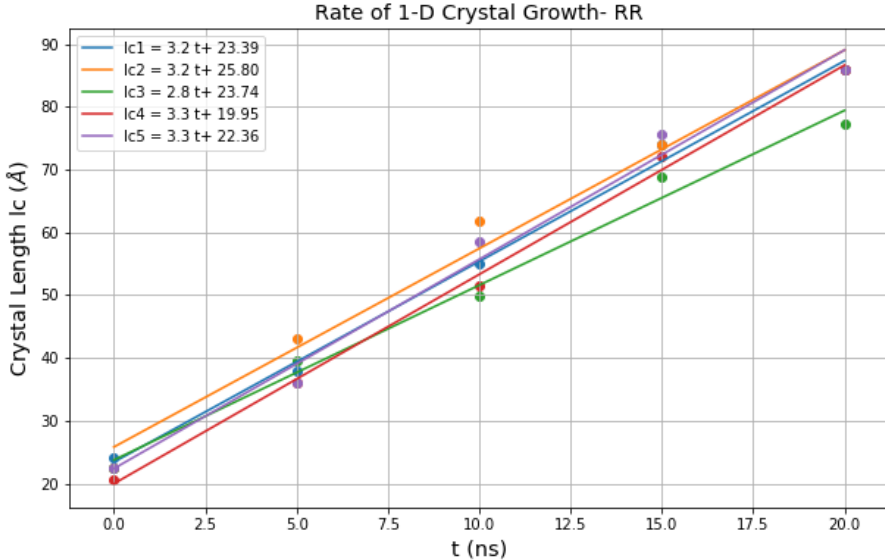


Figure 24: Crystal length evolution vs. time for RR

CG models	rate (m/s)	standard deviation
TraPPE	0.09976	0.00661
RR	0.15824	0.01008

Table 6: Rate of crystal growth for TraPPE and RR

5.3 Crystal Growth Mechanism

From the previous section, the rate of crystal growth is obtained (shown as Table-6). As discussed in section-2, the crystal growth mechanism for N-alkane is a 'slide-in' process. N-alkane molecules initiate the attachment onto the crystal from their chain-end and gradually slide into the crystal (shown as Figure-5). However, this argument is only based on simple observation but is not based on statistical result. Therefore, in this section, an indirect study based on the ALBO ($\overline{Q}_l = \overline{Q}_6$) is done in order to understand the actual process of how a molecule attaches onto the crystal.

During the disorder-order transition, the value of \overline{Q}_6 -s for each beads of octacosane gradually increase. Since it is not a sudden process, there must be a certain portion first attaching onto the crystal which has relatively high \overline{Q}_6 value, and the whole molecule is gradually 'packed' (or slide) into the crystal. For example, in Figure-25, it shows \overline{Q}_6 -s for each beads in molecule no. 139 along the whole simulation. From Figure-25, it can be roughly seen that the crystallization starts at around 3 ns and the crystallization initiates from the end (carbon tag no. 2 – 10). Subsequently the overall \overline{Q}_6 for the whole molecule keeps increasing and converges at around 4.8 ns.

In the example of molecule no. 139, it is noticed that the attachment roughly initiates from its chain-end, which is as discussed in section-2. In order to identify whether chain-end is more likely for crystallization to initiate, multiple molecules should also be taken into consideration. Before doing so, the start and the end of crystallization have to be defined. The definition is shown as Table-7. Here, the crystallization for a molecule starts when there are more than 4 beads, that is, $4/28 \approx 15\%$ of beads in a molecule having $\overline{Q}_6 \geq 0.2$. On the other hand, the crystallization for a molecule ends when there are more than 20 beads, that is, $20/28 \approx 70\%$ of beads in a molecule having $\overline{Q}_6 \geq 0.2$.

Figure-26 shows the \overline{Q}_6 evolution for 20 different molecules as example. Each is shown with their start and end of crystallization. Although 20 different molecules are shown, it is relatively hard to tell whether the crystallization initiates from the end-chain of molecule or not. In order to have a clear representation of which bead is likely to initiate the crystallization (preferred attaching bead site), all the beads with $\overline{Q}_6 \geq 0.2$ when crystallization starts are recorded as the attached beads for all molecules

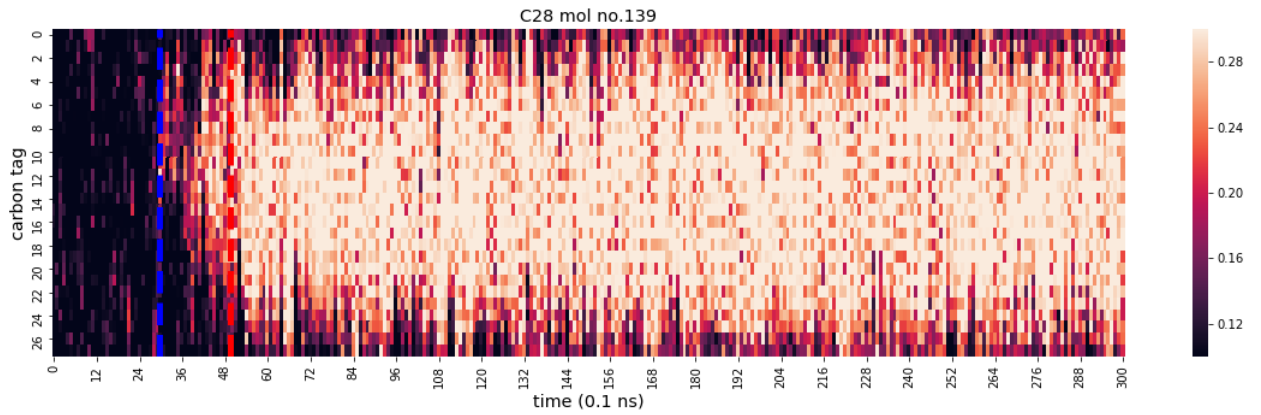


Figure 25: Bead-wise \overline{Q}_6 evolution for example, molecule no. 139

The color-code is on the right side of figure. The color from dark purple to light orange represents \overline{Q}_6 value from low to high. The y-axis represents each carbon number tag for each beads of the octacosane. Carbon tag from 0 to 27 means the (-CH₃)/(-CH₂) bead from one end to the other. Blue dashed line is assumed to be the start of crystallization. Red dashed line is assumed to be the end of crystallization.

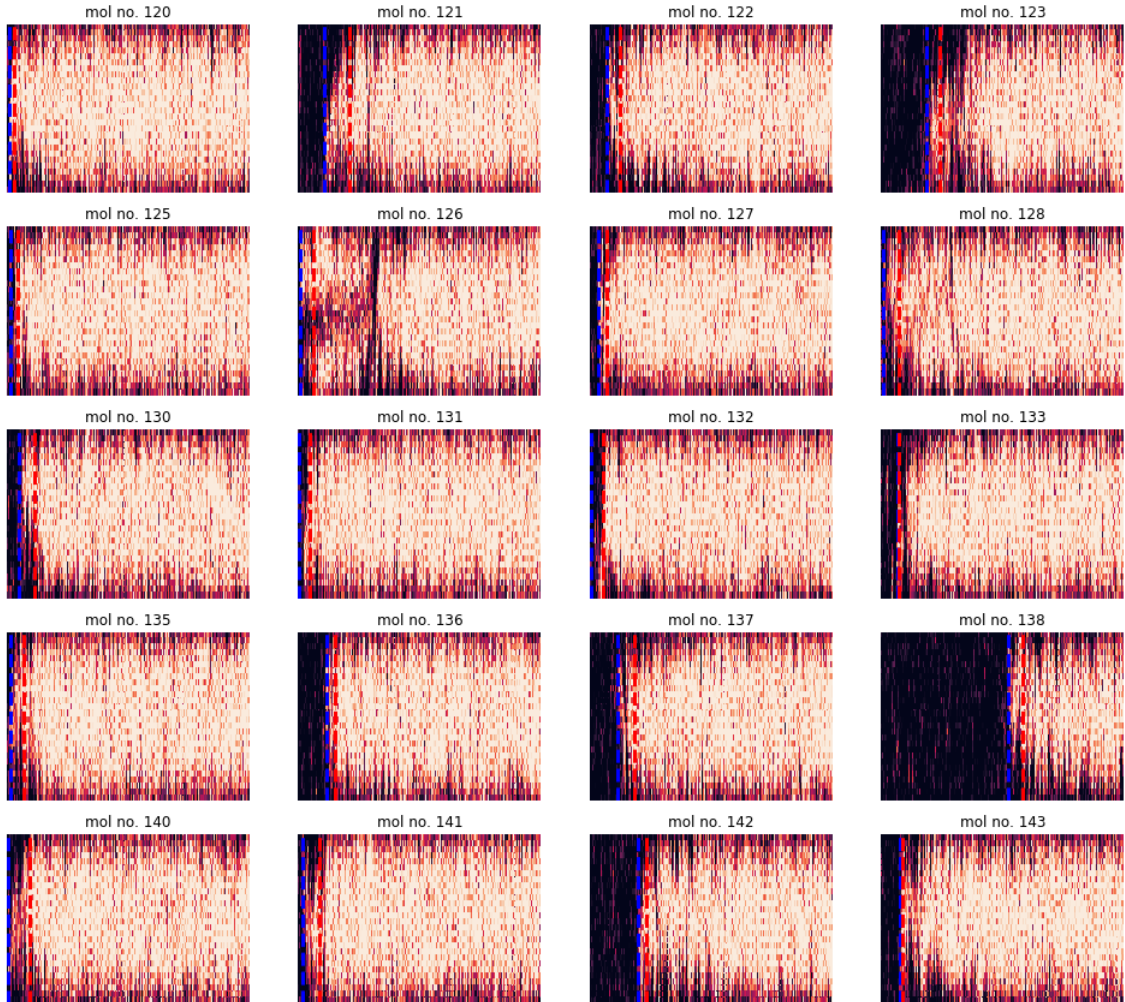


Figure 26: Bead-wise \overline{Q}_6 evolution for example, 20 different molecules

Each block shows one \overline{Q}_6 evolution of one molecule. Blue dashed line is assumed to be the start of crystallization. Red dashed line is assumed to be the end of crystallization.

Event	Definition
Start	when $4/28 (14.28\%)$ of molecule having $\bar{Q}_6 \geq 0.2$
End	when $20/28 (71.42\%)$ of molecule having $\bar{Q}_6 \geq 0.2$

Table 7: Definition for the start/ end of crystallization

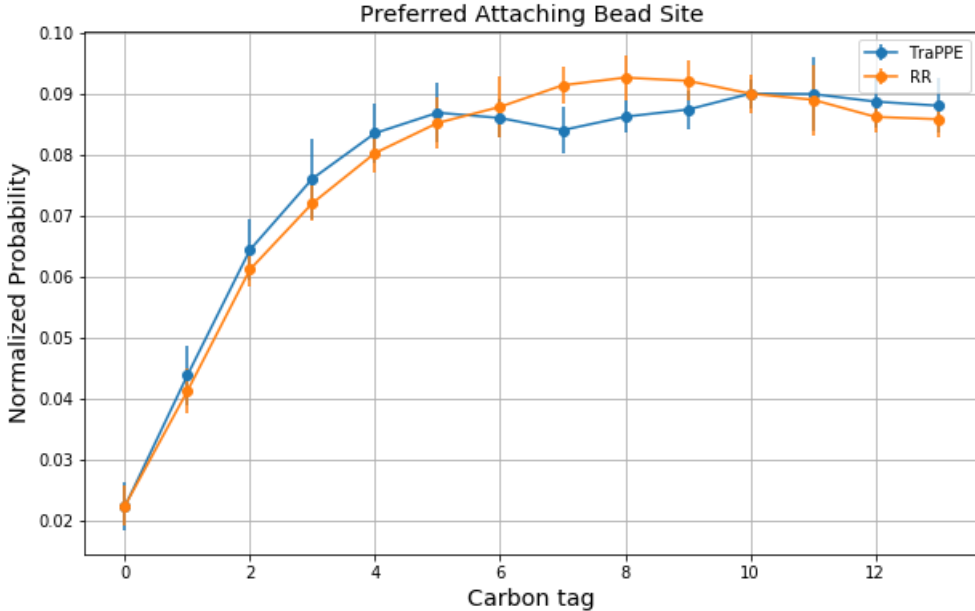


Figure 27: Histogram of preferred attaching bead site for RR and TraPPE; Error-bar represents the standard errors for each corresponding beads

which crystallize at the end. Figure-27 shows the histogram of attached beads. Since the value of \bar{Q}_6 will be higher for those beads crystallized, the histogram of attached beads can be seen as an indirect representation of preferred attaching bead site.

Figure-27 shows two histograms for RR and TraPPE. One should be noted that there are only 14 beads (0-13) in the x-axis. It is because the octacosane molecule is symmetrical with respect to its center, that is, bead i and bead $i+14$ are equivalent. It can be noticed that for the chain-end, the probabilities are close to zero while for the middle, the probabilities show a relative 'plateau'. It clearly contradicts the argument from section-2, which states the attachment is easier to initiate from the chain-ends. The reason may arise from the CG-model or the length of N-alkane molecule. Because ALBO method is not an direct method to study the crystal growth, the mechanism still has to be verified. Nevertheless, it is shown that there is no significant difference in the result of the histogram of attached beads (shown as Figure-27). For both CG-model, the underlying mechanism should be similar.

5.4 Introducing Inhibitors into the System

5.4.1 Inhibitor Density Simulation

So far, some aspects of crystal growth (e.g crystal growth rate and the mechanism) for the pure octacosane system have been explored based on \bar{Q}_6 . It is shown that crystal growth rate is around $9 - 15$ cm/sec, which is relatively fast given the diameters of normal pipelines. In order to solve such problem, many methods have been studied and applied [24]. As discussed in section-1, these methods can be divided into physical and chemical methods. Physical methods include thermal, pigging, magnetic methods and etc. Chemical methods include using crystal modifiers, dispersants and so on [25].

The chemical additives for the prevention of paraffin crystallization can be divided into crystal modifiers (such as crystal growth inhibitors and pour point depressants) and dispersants/ surfactants. The

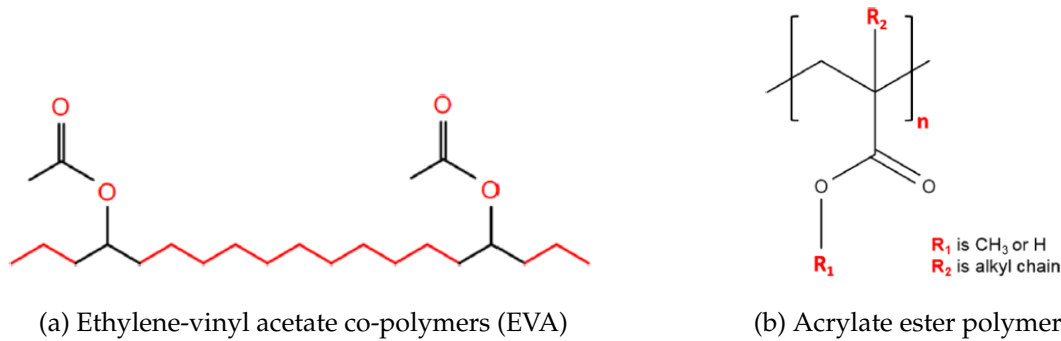


Figure 28: Example inhibitors for (a)linear- / (b)comb- shaped molecule

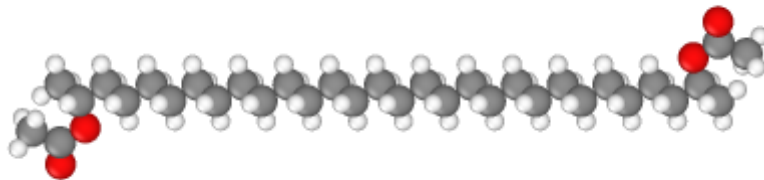


Figure 29: EVA molecule (31.5% vinyl acetate) for the inhibitor simulation

Color-code: Red-Oxygen, Gray-Carbon, White-Hydrogen.

crystal modifiers incorporates themselves into growing crystals and alter their surface characteristics to inhibit deposition. Several crystal modifiers have been evaluated and showed promising results toward crystallization inhibitors which include linear co-polymers and comb-shaped co-polymers. Most linear copolymers are ethylene copolymers, including polyethylene-poly(ethylenepropylene) diblock copolymers, poly(ethylene-butene) polymers (PEB), and ethylene-vinyl acetate co-polymers (EVA) (Figure-28 (a)). Comb-shaped co-polymers include acrylate ester polymers (Figure-28 (b)) and maleic anhydride co-polymers (MAC). Moreover, one important common feature of the above-mentioned crystal modifiers is that they all include crystalline segments that are similar to the N-alkane chains.

Continued from the previous section, in this project, we focus on the simulation on chemical method using crystal modifier EVA. Before considering octacosane-EVA system, pure EVA is first simulated and compared with the experimental data [26] in order to test the transferrability for different CG-models.

• **Method:**

The EVA molecule for simulation is shown as Figure-29 which contains 13 ethylene and 2 vinyl acetate in order to keep the vinyl acetate content of the co-polymer. All the potential coefficients are listed in Table-[8-13]. The simulation includes a pseudo crystal made of 225 EVA molecules in a $60 \times 170 \times 70 \text{\AA}^3$ box. The iterative style is Verlet and the time-step, temperature coupling time, pressure coupling time are 1 fs, 100 fs and 1000 fs respectively. The system is under NPT ensemble where temperature $T = 298K$ and pressure $P = 1 \text{ atm}$ for 1 ns.

• **Result and Discussion:**

The simulation result is shown as Figure-30. The relative error for TraPPE is $(0.956 - 0.922)/0.956 \approx 3.5\%$, which is the lowest value compared with the rest of all CG-models(PCFF, UNIVERSAL, COMPASS, DREIDING). Based on such result, it is shown that TraPPE is transferrable and suitable for the eva simulation.

For the next section, different lengths of EVA molecules will be introduced into the octacosane system. The effect of inhibitor on the crystal will be studied.

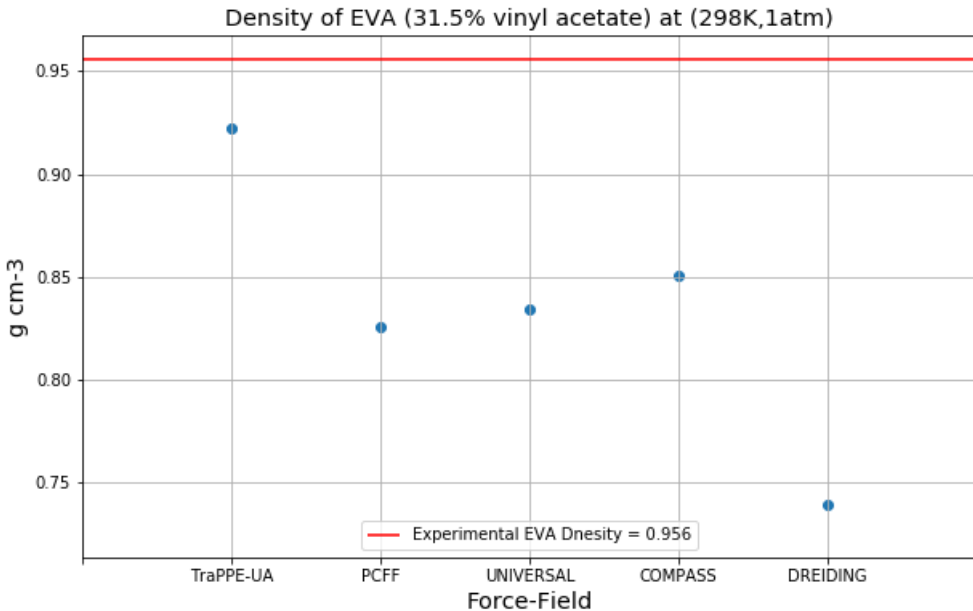


Figure 30: Inhibitor density simulation of EVA (31.5% vinyl acetate) for different CG-models

Trappe Bead type	Abbreviation
$\text{CH}_x\text{-}[\text{CH}_2]\text{-}\text{CH}_x$	CCL
$\text{CH}_x\text{-O-[C]=O}$	CL
$\text{CH}_x\text{-}[\text{CH}_2]\text{-O-CH}_y$	CT2
$[\text{CH}_3]\text{-CH}_x$	CT3
$\text{CH}_x\text{-O-C=O}$	OBL
$\text{CH}_x\text{-O-C=O}$	OCL

Table 8: Details of TraPPE abbreviation for EVA bead type

5.4.2 Effect of Inhibitor on the Octacosane System

After testing TraPPE as a valid CG- model for EVA and octacosane system, the inhibitor simulation is conducted in this section.

- **Method:**

For the simulation set up, the initial configuration is shown as Figure-16, which contains a crystal (160 octacosane molecules) inside the liquid (640 octacosane molecules) in a $52 \times 200 \times 68\text{\AA}^3$ box. Continued from section 5-2, two molecules of two kinds of inhibitors are put randomly into the liquid part of octacosane system respectively. Therefore, there are 802 ($800 + 2$) molecules in total. First inhibitor is EVA molecule with 31.5% vinyl acetate. The other inhibitor is EVA molecule with 29.3 vinyl acetate. Both EVA molecules are shown as Figure-29 and Figure-31. The time-step, temperature coupling time, pressure coupling time are 1 fs, 200 fs and 2000 fs respectively. Verlet iterative style is used. The system is first subject to NPT ensemble ($T = 300\text{K}$ and $P = 1\text{ atm}$) for 0.1 ns. Then, the system is fixed under NPH ensemble and let the system evolves for 30 ns.

- **Result and Discussion:**

Because of the inertness and similarity between EVA and octacosane molecule, the portion, bulkiness of vinyl acetate part and the chain length are the main variables concerning tuning crystallization. It is assumed that by changing the chain length, the crystal morphology and the crystal growth rate may change accordingly. A bulkier, longer inhibitor molecule will result in a lower crystal growth rate. They are both linear molecules which resembles to the octacosane molecule while the main difference lies in their length of ethylene units. EVA with 29.3% vinyl acetate has

Bead type	σ (\AA)	ϵ ($kcal mol^{-1}$)
CCL	3.95	0.0910
CL	3.82	0.0790
CT2	3.95	0.0910
CT3	3.75	0.1947
OBL	3.05	0.1569
OCL	2.80	0.1092

Table 9: Details of TraPPE pair potentials (12-6 LJ potential) for EVA

Bond type	b_0 (\AA)	k_b ($kcal \text{\AA}^{-2} mol^{-1}$)
CT2-CT2	1.54	445.425
CCL-CT3	1.54	445.425
CL-CT3	1.54	445.425
CL-OCL	1.20	1051.00
OBL-CL	1.34	1501.43
OCL-CCL	1.41	1051.00

Table 10: Details of TraPPE bond potentials $k_b(b - b_0)$ for EVA

Angle type	θ_0 (degree)	k_θ ($kcal mol^{-1}$)
CCL-CT2-CT2	114.00	62.1001
CCL-OCL-CL	115.00	62.1001
CT2-CCL-CT3	114.00	62.1001
CT2-CCL-OCL	112.00	49.9782
CT2-CT2-CT2	114.00	62.1001
CT3-CCL-OCL	112.00	49.9782
CT3-CL-OBL	112.00	49.9782
CT3-CL-OCL	112.00	49.9782
OBL-CL-OCL	125.00	62.1001

Table 11: Details of TraPPE angle potentials $k_\theta(\theta - \theta_0)$ for EVA

Dihedral type	k_1 ($kcal mol^{-1}$)	k_2 ($kcal mol^{-1}$)	k_3 ($kcal mol^{-1}$)	k_4 ($kcal mol^{-1}$)
CCL-CT2-CT2-CT2	1.4109	-0.2710	3.1450	0.0000
CT2-CT2-CT2-CT2	1.4109	-0.2710	3.1450	0.0000
CT3-CCL-CT2-CT2	1.4109	-0.2710	3.1450	0.0000
OCL-CCL-CT2-CT2	0.7019	-0.2119	3.0600	0.0000

Table 12: Details of TraPPE dihedral potentials (LAMMPS-opls type potential) for EVA

Dihedral type	m	k_{1-6} ($kcal mol^{-1}$)	n_{1-6}	d_{1-6} (degree)
CT2-CCL-OCL-CL	6	4.034,-1.494,-1.071,-0.043,-0.101,1.323	0,1,2,3,4,0	0,0,0,0,0,0
CT3-CCL-OCL-CL	6	4.034,-1.494,-1.071,-0.043,-0.101,1.323	0,1,2,3,4,0	0,0,0,0,0,0
CT3-CL-OCL-CCL	6	4.034,-1.494,-1.071,-0.043,-0.101,1.323	0,1,2,3,4,0	0,0,0,0,0,0
OBL-CL-OCL-CCL	6	3.618,-0.829,-2.728,-0.059, 0.000,0.000	0,1,2,3,4,0	0,0,0,0,0,0

Table 13: Details of TraPPE dihedral potentials (LAMMPS-fourier type potential) for EVA

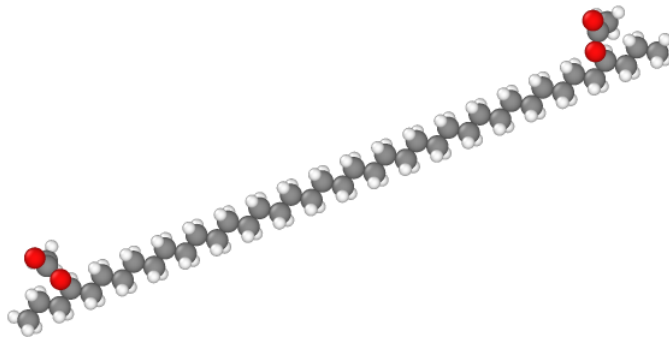


Figure 31: EVA molecule (29.3% vinyl acetate) for the inhibitor simulation

Color-code: Red-Oxygen, Gray-Carbon, White-Hydrogen.

EVA molecule	vinyl acetate unit	ethylene unit (position)
EVA with 29.3% vinyl acetate	18.5	2.5 (back bone carbon 2, 29)
EVA with 31.5% vinyl acetate	13	2 (back bone carbon 4, 38)

Table 14: Comparison between two EVA inhibitor molecules

a longer linear backbone. Their comparison is also summarized in Table-14. The snapshots of simulation result for both inhibitors are shown as Figure-32 and Figure-33. From the figures it can be seen that both molecules are eventually incorporated into the crystal. Figure-34 shows the \overline{Q}_6 coloring for Figure-33. It shows EVA with 29.3 vinyl acetate changes the direction of crystal growth because its chain is long enough to 'mass up' the crystal orientation. It is as our assumption that the crystal may change when the inhibitor molecule becomes longer. However, for both EVA inhibitors, there are basically no changes in the crystal growth rate. But it should be noted that there is only one sample for each simulation which may not be statistically valid to draw any conclusion.

6 Conclusion

In this project, first we choose the pure octacosane ($C_{28}H_{58}$) to model crude oil system for simplicity. We compared three CG-models (RR, DR and TraPPE-UA) based on liquid density, melting point and calculation performance. TraPPE-UA is considered the best CG-model because it not only has an acceptable performance given the system of interest, the lowest error for all properties we have tested, but also is transferable across a variety of elements. Later, averaged local bond order parameter with $l = 6$ (ALBO, \overline{Q}_6) is applied in order to study the crystal process, including crystal growth and crystallization mechanism. It is found that the crystallization does not mainly initialize from the chian-end against the argument from previous study and that the crystal growth rate is around 15 cm/sec. Finally, two inhibitors (EVA with 31.5% and 29.3% vinyl acetate) are introduced into the system. Surprisingly, the crystal growth rate does not change accordingly but the direction of crystal growth changes for a longer chain. In this project, all the conclusions are not assertive since the simulation needs more samples to have a more statistical meaning and the ALBO method is not a direct way to study crystallization.

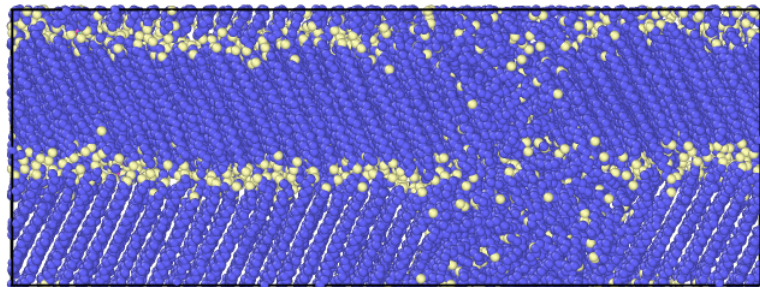


Figure 32: Snapshot of EVA molecule (31.5% vinyl acetate) at 30 ns

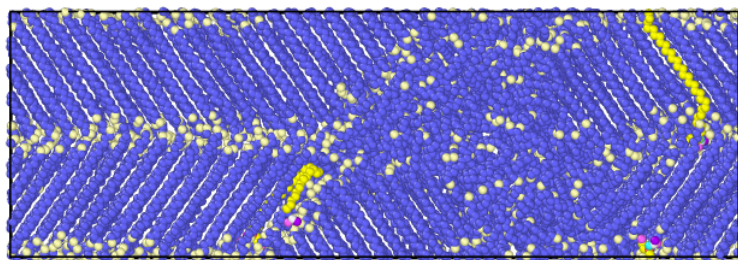


Figure 33: Snapshot of EVA molecule (29.3% vinyl acetate) at 30 ns

The molecule with colors of yellow, purple, pink, light blue is EVA molecule.

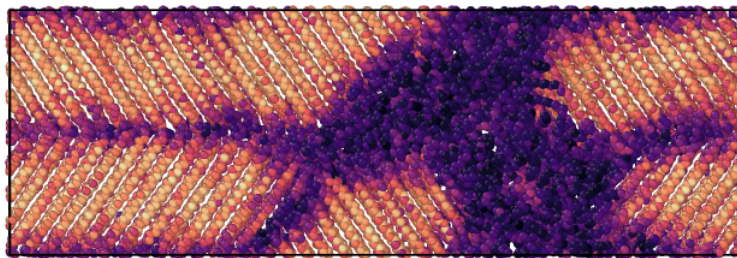


Figure 34: \overline{Q}_6 colored snapshot of EVA molecule (29.3% vinyl acetate) at 30 ns

References

- [1] N. X. Thanh, M. Hsieh, and R. Philp, "Waxes and asphaltenes in crude oils," *Organic Geochemistry*, vol. 30, no. 2-3, pp. 119–132, 1999.
- [2] S. Plimpton, "Fast parallel algorithms for short-range molecular dynamics," *Journal of computational physics*, vol. 117, no. 1, pp. 1–19, 1995.
- [3] S. R. Craig, G. P. Hastie, K. J. Roberts, and J. N. Sherwood, "Investigation into the structures of some normal alkanes within the homologous series c13h28 to c60h122 using high-resolution synchrotron x-ray powder diffraction," *Journal of Materials Chemistry*, vol. 4, no. 6, pp. 977–981, 1994.
- [4] E. Sirota, "Supercooling, nucleation, rotator phases, and surface crystallization of n-alkane melts," *Langmuir*, vol. 14, no. 11, pp. 3133–3136, 1998.
- [5] N. Wentzel and S. T. Milner, "Crystal and rotator phases of n-alkanes: A molecular dynamics study," *The Journal of Chemical Physics*, vol. 132, no. 4, p. 044901, 2010.
- [6] E. Sirota and A. Herhold, "Transient rotator phase induced nucleation in n-alkane melts," *Polymer*, vol. 41, no. 25, pp. 8781–8789, 2000.
- [7] A. Taggart, F. Voogt, G. Clydesdale, and K. Roberts, "An examination of the nucleation kinetics of n-alkanes in the homologous series c13h28 to c32h66, and their relationship to structural type, associated with crystallization from stagnant melts," *Langmuir*, vol. 12, no. 23, pp. 5722–5728, 1996.
- [8] M. Anwar, F. Turci, and T. Schilling, "Crystallization mechanism in melts of short n-alkane chains," *The Journal of chemical physics*, vol. 139, no. 21, p. 214904, 2013.
- [9] N. Wentzel and S. T. Milner, "Simulation of multiple ordered phases in c23 n-alkane," *The Journal of chemical physics*, vol. 134, no. 22, pp. 224–504, 2011.
- [10] J. C. Shelley, M. Y. Shelley, R. C. Reeder, S. Bandyopadhyay, P. B. Moore, and M. L. Klein, "Simulations of phospholipids using a coarse grain model," *The Journal of Physical Chemistry B*, vol. 105, no. 40, pp. 9785–9792, 2001.
- [11] W. L. Jorgensen and J. Tirado-Rives, "The opls [optimized potentials for liquid simulations] potential functions for proteins, energy minimizations for crystals of cyclic peptides and crambin," *Journal of the American Chemical Society*, vol. 110, no. 6, pp. 1657–1666, 1988.

- [12] S. J. Marrink, H. J. Risselada, S. Yefimov, D. P. Tieleman, and A. H. De Vries, "The martini force field: coarse grained model for biomolecular simulations," *The journal of physical chemistry B*, vol. 111, no. 27, pp. 7812–7824, 2007.
- [13] T. Vettorel and H. Meyer, "Coarse graining of short polyethylene chains for studying polymer crystallization," *Journal of chemical theory and computation*, vol. 2, no. 3, pp. 616–629, 2006.
- [14] S. L. Mayo, B. D. Olafson, and W. A. Goddard, "Dreiding: a generic force field for molecular simulations," *Journal of Physical chemistry*, vol. 94, no. 26, pp. 8897–8909, 1990.
- [15] C. Luo, J.-U. Sommer, E. Schreiner, I. G. Castro, J. Tinsley, and H. Weiss, "Length-dependent segregation in crystallization of n-alkanes: Md simulations," *Journal of Non-Crystalline Solids*, vol. 407, pp. 206–212, 2015.
- [16] K. A. Maerzke and J. I. Siepmann, "Transferable potentials for phase equilibria- coarse-grain description for linear alkanes," *The Journal of Physical Chemistry B*, vol. 115, no. 13, pp. 3452–3465, 2011.
- [17] T. Yamamoto, "Molecular dynamics modeling of polymer crystallization from the melt," *Polymer*, vol. 45, no. 4, pp. 1357–1364, 2004.
- [18] M. G. Martin and J. I. Siepmann, "Transferable potentials for phase equilibria. 1. united-atom description of n-alkanes," *The Journal of Physical Chemistry B*, vol. 102, no. 14, pp. 2569–2577, 1998.
- [19] D. M. Duffy and P. M. Rodger, "Modelling the interaction between the poly(octadecyl acrylate) inhibitor and an n-octacosane crystal," *Physical Chemistry Chemical Physics*, vol. 2, no. 20, pp. 4804–4811, 2000.
- [20] R. A. Scott and H. A. Scheraga, "Conformational analysis of macromolecules. II. the rotational isomeric states of the normal hydrocarbons," *The Journal of Chemical Physics*, vol. 44, pp. 3054–3069, Apr. 1966.
- [21] K. D. Papavasileiou, L. D. Peristeras, A. Bick, and I. G. Economou, "Molecular dynamics simulation of pure n-alkanes and their mixtures at elevated temperatures using atomistic and coarse-grained force fields," *The Journal of Physical Chemistry B*, vol. 123, pp. 6229–6243, June 2019.
- [22] S. Sastry and C. A. Angell, "Liquid–liquid phase transition in supercooled silicon," *Nature materials*, vol. 2, no. 11, p. 739, 2003.
- [23] P. J. Steinhardt, D. R. Nelson, and M. Ronchetti, "Bond-orientational order in liquids and glasses," *Physical Review B*, vol. 28, pp. 784–805, July 1983.
- [24] M. K. Siljuberg, "Modelling of paraffin wax in oil pipelines," Master's thesis, Institutt for petroleumsteknologi og anvendt geofysikk, 2012.
- [25] Y. Chi, J. Yang, C. Sarica, and N. Daraboina, "A critical review of controlling paraffin deposition in production lines using chemicals," *Energy & fuels*, vol. 33, no. 4, pp. 2797–2809, 2019.
- [26] I. Díaz, E. Díez, J. Camacho, S. León, and G. Ovejero, "Comparison between three predictive methods for the calculation of polymer solubility parameters," *Fluid Phase Equilibria*, vol. 337, pp. 6–10, 2013.